# Nuclear modification of charged-particle production at $\sqrt{s_{ m NN}}=5.02$ TeV in ALICE

**Master's Thesis** Institut für Kernphysik Frankfurt

#### Youssef El Mard Bouziani

Fachbereich Physik Goethe-Universität Frankfurt am Main

13th September 2021

Erstgutachter: Prof. Dr. Henner Büsching Zweitgutachter: Prof. Dr. Harald Appelshäuser

# **Contents**

0	Abs	tract		1		
1	The	oretical	Background	3		
	1.1	The Str	ructure of Matter	3		
	1.2	Quantı	um Chromodynamics	6		
	1.3	The Qu	ıark-Gluon plasma	7		
			The bag model	7		
			The QCD phase diagram	8		
			Evolution of heavy-ion collisions	9		
	1.4		n production in hard collisions	11		
	1.5		Energy Loss	13		
	1.6	Charge	ed-particle Spectra and Nuclear Modification Factors	14		
2	The	ALICE	Experiment at CERN	17		
	2.1	The LH	HC	17		
	2.2	ALICE		18		
		2.2.1	Inner Tracking System	20		
		2.2.2	Time Projection Chamber	20		
		2.2.3	V0 detector	22		
		2.2.4	Track reconstruction	23		
		2.2.5	Transverse momentum and momentum resolution	24		
		2.2.6	Centrality estimation	25		
3	Analysis 2					
	3.1	Data sa	ample	28		
	3.2	Trigger	and event selection	29		
		3.2.1	Trigger	29		
		3.2.2	Selection of events	30		
	3.3	Track s	selection	31		
	3.4	Corrections				
		3.4.1	Overall normalization	34		

		3.4.2	Signal loss	35				
		3.4.3	Tracking efficiency and acceptance	36				
		3.4.4	Contamination by secondary particles	42				
		3.4.5	Transverse momentum resolution	47				
	3.5	Imple	mentation of the corrections	52				
	3.6	System	natic uncertainties	53				
		3.6.1	Track selection	53				
		3.6.2	Other sources of uncertainties	55				
	3.7	Result	ts	57				
		3.7.1	Differential cross section in pp collisions	57				
		3.7.2	Invariant yield in Pb-Pb collisions	58				
		3.7.3	Nuclear modification factors	60				
4	Sun	nmary		64				
Aı	peno	dices		66				
A	A Kinematic variables							
Bi	Bibliography							

#### 0 Abstract

In the first fractions of a second after the Big Bang, the fundamental constituents of matter, namely quarks and gluons, behaved like quasi-free particles in a state of matter at high energy densities known as quark-gluon plasma (QGP). Shortly thereafter, the expansion of the universe and the resulting cooling of the matter yielded to the formation of bound quark states, called hadrons, as for example protons and neutrons that make up atom nuclei. The strong interaction, one of the four fundamental interactions, is responsible for the formation of composite particles. The theory of the strong interaction, named quantum chromodynamics (QCD), predicts that quarks and gluons can't exist outside bound states under ordinary conditions, which reflects the exceptional nature of the QGP. Besides the Big Bang, this exotic state of matter is believed to be located in the inside of neutron stars where the required extreme conditions are met.

Since its theoretical proposal forty years ago, the QGP has been a subject of huge interest in the field of high-energy physics, given that it could offer answers to fundamental questions about the structure of matter. For the study of the QGP, the conditions for the creation of a QGP must be reproduced in research facilities. This is accomplished accelerating heavy ions close to the speed of light and causing them to collide. The resulting energy densities allow for a briefly formation of a QGP in a controlled environment. Immediately afterwards, the medium cools down and multiple particles are produced. The study of these particles enables conclusions to be drawn on the QGP.

The ALICE experiment is dedicated to the study of particles produced in ultrarelativistic heavy-ion collisions provided by the CERN LHC, the world's largest particle accelerator. In this work, the charged-particle production in lead-lead (Pb-Pb) collisions is investigated. According to the current state of knowledge, the particle production in this collision system is presumably affected by the influence of the hot QGP medium. Therefore, a comparison of the production of charged particles in Pb-Pb collisions to the one in pp collisions, where no formation of QGP is expected, could reveal modifications caused by the QGP. The charged-particle productions are presented as function of the transverse momentum  $p_{\rm T}$ . The comparison between the  $p_{\rm T}$  distributions from pp and Pb-Pb collisions is quantified by the so-called nuclear modification factor  $R_{AA}$ . In particular, the in-medium modification of the particle production should manifest with a nuclear modification factor  $R_{AA} < 1$ .

In this thesis, the measured  $p_T$  distribution of non-identified charged particles in pp and Pb-Pb collisions at a centre-of-mass energy of  $\sqrt{s_{\mathrm{NN}}} = 5.02 \, \mathrm{TeV}$  as well as the resulting nuclear modification factors are reported. This analysis of  $R_{\rm AA}$  draws upon the increased statistics, specially in pp collisions, with respect of the previous ALICE measurement presented in [AAA+18]. This increase is expected to be reflected in an enlarged  $p_T$  reach of the charged-particle  $p_T$  distribution and, in turn, in the  $p_T$  reach of the nuclear modification factors. This thesis is structured as follows. In Chapter 1, the theoretical background that leads to the description of the mechanisms responsible for the modification of the particle production due to in-medium effects is introduced. Next, Chapter 2 gives a general introduction to the detectors of the ALICE experiment with a particular emphasis on the reconstruction of charged particles trajectories. In Chapter 3, the analysis methods used for the calculation of the fully corrected  $p_{\rm T}$  distributions and the  $R_{\rm AA}$  are presented. In this chapter, the obtained  $R_{\rm AA}$  is compared to theoretical predictions. Finally, Chapter 4 contains a summary of the thesis.

# 1 Theoretical Background

#### 1.1 The Structure of Matter

Throughout the twentieth century, successive crucial advances in the field of particle physics led to a revolution of the world-view on the structure of matter and the fundamental forces that govern the universe. Following these developments, it became necessary to consolidate the acquired knowledge into a single theory: the Standard Model, which marked by the end of the 1970s the foundation of modern particle physics. This systematization provided from a theoretical point of view subsequently confirmed experimentally a comprehensive description of the nature of elementary particles and the fundamental interactions they mediate: the electromagnetic, the weak and the strong interaction.

All matter in the universe is composed of indivisible particles that lack spatial extent and substructure, the so-called elementary particles. The first particles to be proposed as elementary were the atoms. This picture changed in the early 20th century after it was proved that atoms are made up of a nucleus constituted by protons and neutrons, around which electrons orbit. In the subsequent decades, an extensive number of other subatomic particles were discovered, raising the question among physicists of whether all of them were in fact structureless. The Standard Model sorted out this confusion, historically known as particle zoo, describing the existence of a low number of elementary particles subdivided into two types named quarks and leptons that build all known particles, including protons and neutrons. In addition, the Standard Model clarified that the interactions between quarks and leptons occur by means of an exchange of force-carrier particles, also considered elementary.

The most fundamental distinction between the building blocks of matter and the force-carrier particles lies in the intrinsic angular momentum, known generally as spin, all particles carry, whether or not they are elementary. Particles of half-integer spin in units of the Planck's constant  $\hbar$  are named fermions and present an antisymmetric wave function, whereas those of integer spin are known as bosons and their wave function describes a symmetric behavior. In this context,

quarks and leptons are considered elementary fermions, while the force-carriers are referred to as gauge bosons.

The Standard Model states the existence of six quarks and six leptons, summarized in Figure 1.1. Both groups of elementary fermions are arranged according to the mass in three doublets named generations. Each pair of quarks or leptons have a mass one or two orders of magnitude lower than the pair of the next generation. Furthermore, the triplets composed of elementary fermions from different generations have the same electrical charge. The Standard Model predicts also the occurrence of antiquarks and antileptons, elementary fermions with identical mass as their counterparts but opposite electrical charge and spin. The six species or flavours of quarks known at the present day are up u, down d, charm c, strange s, top t and bottom b. At this point, it should be emphasized that quarks could not yet be observed existing on their own, but only building bound states named hadrons. These composite particles, detected for the first time during the era of the particle zoo, come in two types: hadrons built from three different quarks are called baryons, while those constituted of a quark-antiquark pair mesons. For instance, the quark composition of protons and neutrons, respectively *uud* and *udd*, allows to identify them as baryons. All known hadrons, excluding the proton, decay after a given period of time. It should be also noted that since the spin is an additive property, baryons are considered fermionic particles and mesons, by contrast, bosonic particles.

The quark composition of a hadron determines intrinsic facets of the particle, as for example the electrical charge. However, the valence quarks, i.e. the quarks that determine the identity of a hadron, aren't the only components. In fact, a hadron should be understood as a more complex and dynamic structure that contains, aside from the valence quarks, an amalgam of quark-antiquark pairs named sea quarks in a constant process of creation and annihilation as well as a large number of gluons, the force-carrier of the strong interaction. This picture is consistent with the fact that the sum of the masses of the valence quarks of a given hadron doesn't coincide with the observed mass of the hadron, being this significantly larger.

As already mentioned, six flavours of leptons are known at this time: three electrically charged leptons, the electron e, the muon  $\mu$  and the tau  $\tau$ , and the corresponding electrically neutral leptons that complete each generation, the electron neutrino  $v_e$ , the muon neutrino  $v_\mu$  and the tau neutrino  $v_\tau$ . In contrast to quarks, leptons exist on their own, with the big exception of the electron shell of an atom.

According to our actual understanding, all observed phenomenon at subatomic level, such as the formation of composite particles or the particle decays, man-

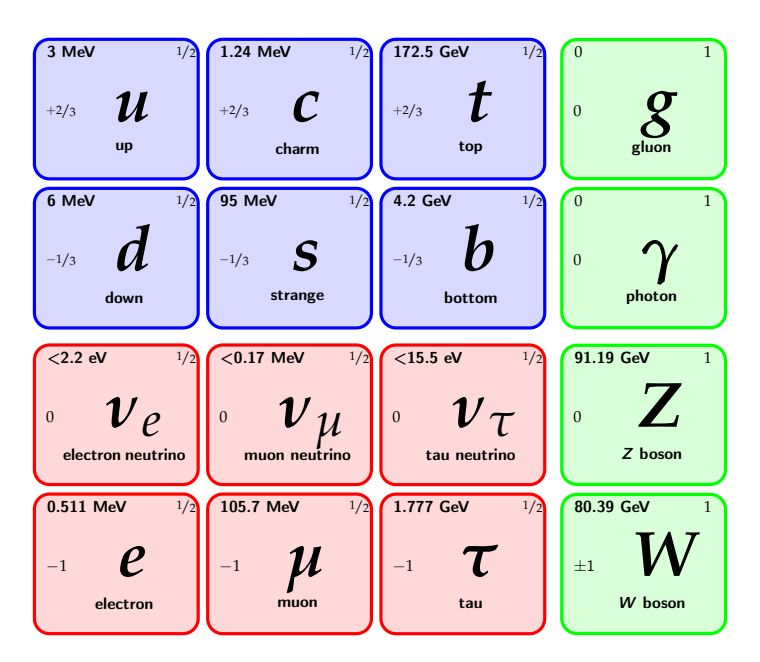


Figure 1.1: Elementary particles of the Standard Model. Quarks, leptons and force carriers are presented in blue, red and green, respectively. The mass, the spin and the electric charge are found in the upper left, upper right and bottom left of each cell, respectively [T<sup>+</sup>18].

ifest themselves by means of the existence of three fundamental interactions: the electromagnetic, the weak and the strong interaction. In modern particle physics, each of these interactions is explained as an exchange of quanta of elementary bosons between the elementary particles that exert the force. In order to experience a given fundamental force, an elementary particle must carry the corresponding charge. Particles are charged in different magnitudes, which determines the intensity with they create or undergo the force.

The force-carrier particle of the electromagnetic interaction is named photon  $\gamma$ , a massless boson that mediates the attraction and repulsion forces between all electrically charged particles. In the case of the weak interaction, which all elementary fermions can experience, there are three massive mediators: one electrically neutral, namely the Z boson, and two electrically charged, the  $W^\pm$  bosons. Finally, the strong interaction is mediated by the already introduced gluon g. The charge of the strong interaction is called color, but it should not be mistaken for the concept generally known and described by the optical physics. Quarks are the only elementary fermions that have color charge and therefore gluons can couple to them. In addition to quarks, gluons carry also color what allows them to couple to themselves, a particularity only present in the strong interaction. The basic processes of the strong interaction are described by a theory named quantum chromodynamics (QCD). Since some of these processes represent a key knowledge for the understanding of this thesis, this theory will be

treated in the coming section more exhaustive.

#### 1.2 Quantum Chromodynamics

Historically, the concept of colors were introduced in order to remedy an apparent violation of the Pauli's exclusion principle, which states the antisymmetric nature of hadrons. During the early development of the quark model, the wave function of hadrons appeared to be symmetric. This fact led to propose the existence of the color charge, a new quantum state, which guaranteed to explain the antisymmetric behavior of hadrons. In the QCD theory, three types of color charge, namely red (r), blue (b) and green (g), are defined. Quarks take one kind of color, while antiquarks are charged with the matching anticolors. In contrast to the electric charge, the color of quarks can be modified in fundamental processes of the strong interaction, where gluons play the role of mediators. To ensure the conservation of the color charge, gluons must carry thus a coloranticolor pair. According to the combinations predicted by the formalisms of the SU(3), the symmetry group of the QCD, eight distinct types of gluons exist in nature.

In the framework of the color-force field, quarks are found in nature only forming hadron bound states. This phenomenon, known as confinement, can be disentangled by considering the attractive potential V between a quark-antiquark pair. At distances of the order 1 fm, the potential behaves analogously to the Coulomb potential of the QED, i.e. it scales with the inverse of the radius r between the particles. Beyond this range, the quark-antiquark pair remains also confined in the bound state. In addition, a linear term must be assumed in order to ensure the observed increasing trend of the potential. It therefore follows [Bü18]:

$$V(r) = -\frac{4}{3} \frac{\alpha_{\rm S}}{r} + kr \tag{1.1}$$

where  $\alpha_s$  represents the QCD coupling constant and k the so-called string tension, which is measured experimentally. Considering Equation 1.1, pulling the quark-antiquark pair to greater lengths r should lead to an attenuation of the attractive potential. Nevertheless, the energy required for this would eventually be sufficient to create a new quark-antiquark pair which retains the original pair in a confined state as shown schematically in Figure 1.2.

A detailed look at the Coulomb term of the potential provides a different perspective of the quark coupling. At this point, the concept of running coupling constant must be introduced. The QCD coupling constant  $\alpha_s$  is in fact not really an invariant quantity, but it depends logarithmically on the momentum transfer

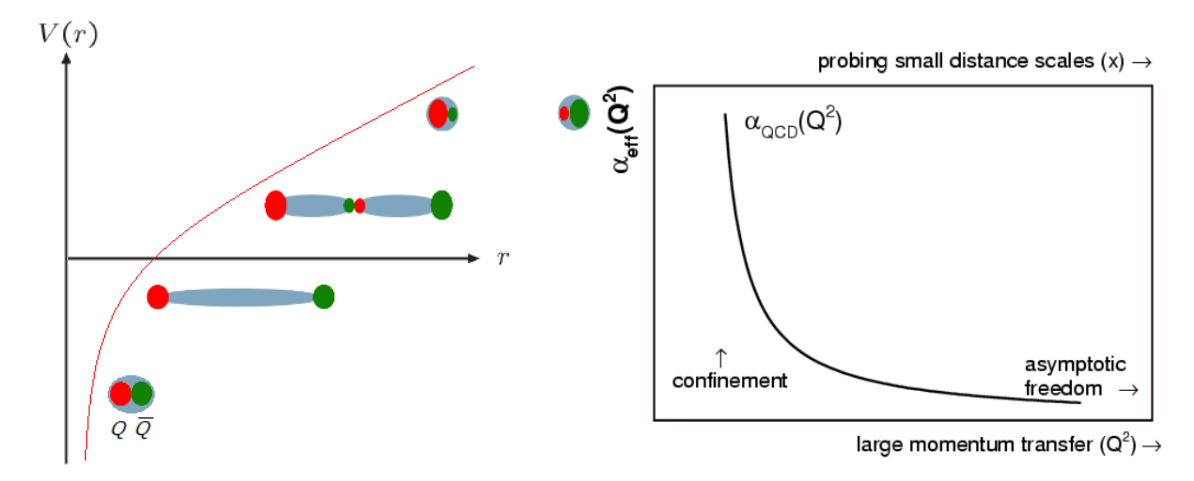


Figure 1.2: **Left:** QCD potential as function of the radius along with a sketch of the hadronisation of a quark-antiquark pair by increasing distance. Figure adapted from [Che10]. **Right:** Running coupling constant of the QCD as function of the momentum transfer [Bü18].

Q between the particles as follows [Bü18]:

$$\alpha_{\rm s} \propto \frac{1}{\ln \frac{Q^2}{\Lambda_{\rm OCD}^2}}$$
 (1.2)

where  $\Lambda_{\rm QCD}^2$  is the QCD scale parameter. In Figure 1.2, a sketch of the running coupling constant of the QCD is shown af function of the momemntum transfer. As a consequence, increasing momentum transfers, which according to the De Broglie relation imply short distances, should result in a weakened QCD potential, a phenomenon called asymptotic freedom. At this stage, quarks in bound states overcome the confinement and exist as free particles. This feature in QCD also applies for the gluon coupling. In particle physics, the state of matter in which quarks and gluons are liberated from the confinement state and thus free color charges are allowed is known as quark-gluon plasma (QGP). Since the problem statement of this thesis is built around the study of the QGP, the next section is focused on this exotic state of matter.

#### 1.3 The Quark-Gluon plasma

#### 1.3.1 The bag model

The transition of hadronic matter to a QGP can be described in a simplified form by the so-called bag model [CJJ<sup>+</sup>74]. According to the model, the QCD vacuum operates as an ideal conductor. Hadrons are presented as finite regions from this

space, called bags, which present a constant energy density. By that, the confinement of the chromoelectric and chromomagnetic fields inside the bags can be stated. Furthermore, the boundary conditions of the quark wave-function ensure the confinement of the quarks inside the bags [BMW06].

The bag model provides an answer to the fundamental question about the evolution of the hadron structure when the temperature is increased. Under this condition, it proposes the decay of atomic nuclei to their nucleons. From the vacuum, light hadrons, primarily pions, originate and fill the space. Towards a certain limit temperature  $T_c$ , the amalgam of light hadrons and nucleon bags start to overlap reducing thus the distance between the constituent particles and, by that, entering the regime of the asymptotic freedom. After overcoming the limit temperature, quarks and gluons move freely as deconfined states through a QGP. Likewise, this phase transition is also suggested for the case of increasing particle density, which give rise to a cold QGP after reaching a critical value.

#### 1.3.2 The QCD phase diagram

The phase evolution of strongly interacting matter could not yet be proven either experimentally or theoretically. Nevertheless, different graphical representations of the corresponding phase diagram have been conjectured over the years. In Figure 1.3, a phase diagram which summarizes the knowledge about the QCD phases as of today is presented. The axes correspond to the temperature and the net baryonic density. Two distinct regions can be distinguished in the phase diagram, namely a confined state of matter and the QGP regime, both separated by a hypothetically phase transition. In addition, a critical end point (CEP), above which the phase boundaries disappear, is suggested by a lattice formulation of the QCD. At vanishing baryon densities, a rapid cross-over between phases is expected in which no distinction between states of matter can be made. Towards higher baryon densities, the transition becomes less subtle and the transition continuous.

The phase diagram includes also the two speculated scenarios for the formation of a QGP in nature. At the present time, it is assumed that the primordial universe ( $< 10^{-6}$  s) was under temperatures high enough that led to the existence of a QGP. The subsequently expansion of the universe yielded to a cooling of the matter which transited then to a hadronic gas, before reaching the current ordinary state. The second example of QGP in nature is supposed to be located in the inside of neutron stars, where the extreme density enables the overlap of elementary particles. It becomes therefore clear the extreme conditions matter must undergo to create a QGP. To investigate the QGP in a controllable medium,

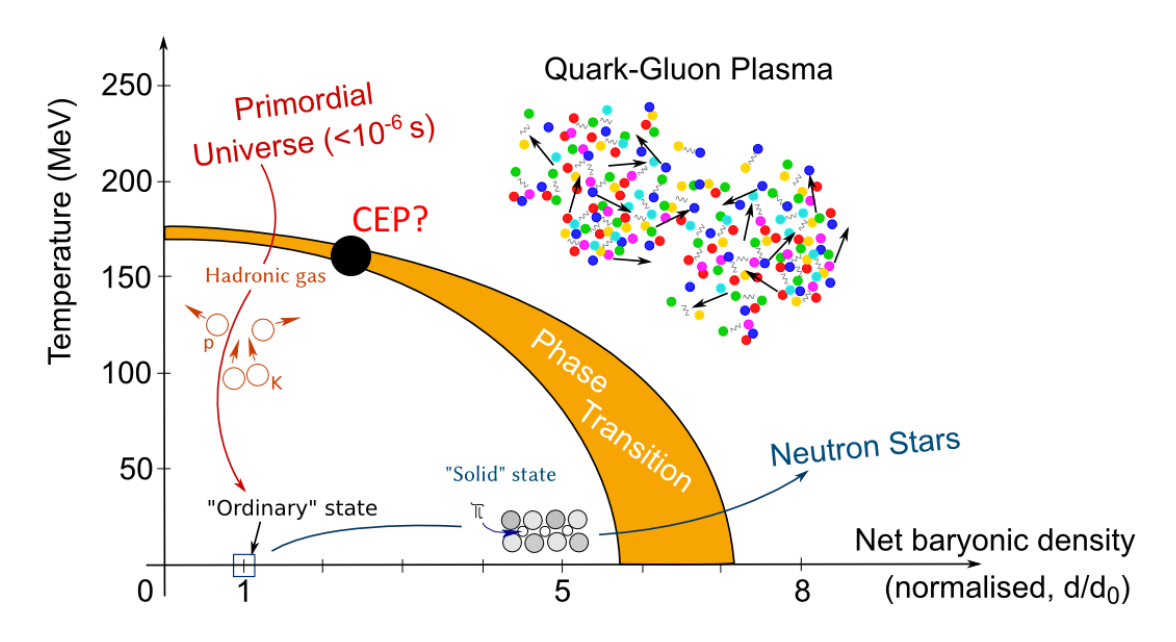


Figure 1.3: Conjectured phase diagram of strongly interacting matter [Mai15].

the required energy densities are reproduced in heavy-ion collisions.

#### 1.3.3 Evolution of heavy-ion collisions

In high energy physics, the QGP is probed through ultra-relativistic heavy-ion collisions which concentrate high energies in a limited volume. In Figure 1.4, the evolution of a heavy-ion collisions, depicted in this section, is represented in a spacetime diagram. Due to the relativistic acceleration, the hadrons inside the heavy ions undergo a geometrical Lorentz contraction and a dilation of the internal timescales [GEL13]. The later effect causes that the constituent quarks and gluons, called partons, can not longer interact precisely and appear to be deconfined. An additional consequence is the dilation of the lifetime of the strong processes inside the hadron, which results in an increase of the gluon density proportional to the collision energy. Gluons outnumber then the valence and sea quarks and the state comes to a gluon saturation. This stage previous to the collision is described in the framework of the so-called Color Glass Condensate (CGC), which uses a classical field approach for the description of the system. The initial stage of a collision between two nuclei should be therefore understood as the clash of two sheets defined by the CGC formalism [Ven08]. The corresponding classical fields change from a configuration transverse to the beam direction and confined inside the sheets to a longitudinal color electomagnetic field that connects both sheets. During this new configuration, known as glasma, the energy density increases until partons are released and they assume the role of degrees of freedom of the collision. The glasma is considered an intermediate

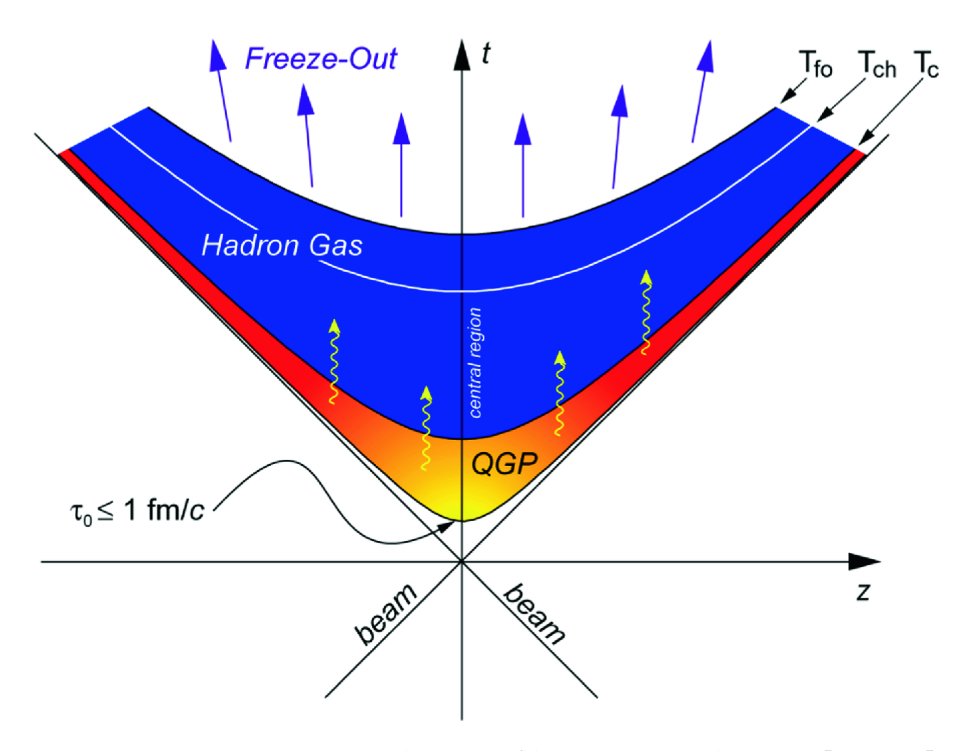


Figure 1.4: Spacetime evolution of heavy-ion collisions [Agg21]

stage with both CGC and QGP properties and its description is unavoidable to quantify the initial conditions for the creation of the QGP.

As the system evolves, inelastic interactions between partons arise. Consequently, the initial targets slow down and the dilation of the internal time scales dissipate. At this stage, the system can experience a thermodynamically equilibrium that leads to the formation of the QGP [Bü18]. Immediately after this, the system expands and, by that, the temperature declines crossing eventually the critical limit  $T_c$ , which yields to the hadronization of the system. The resulting hadron gas continues with the expansion and the corresponding cooling or freeze-out. This happens in two phases, namely the chemical freeze-out at  $T_{\rm ch}$ , in which inelastic collisions stop and the hadron abundances are established, and the kinetic freeze-out at  $T_{fo}$ , from which the elastic interactions cease and the momentum distributions remain invariant [Bü18]. The freeze-out phase is of great relevance since it provides insight on the properties of the QGP. There are several signatures to study the QGP, e.g. the electromagnetic and hadronic radiation, the dissociation of quarkonia<sup>1</sup> or the parton energy loss. Since the last observable occupies a central position in this thesis, it will be covered in detail later on. Before this, the particle production of the final state should be addressed.

<sup>&</sup>lt;sup>1</sup>Mesons composed of a heavy quark-antiquark pair with the same flavour

#### 1.4 Hadron production in hard collisions

Due to the small time scales of the QCD hot medium, its signatures must be examined analyzing the hadrons produced in ultra-relativistic heavy-ion collisions. Thus, it turns out useful to compare the particle production in such conditions to the one created in a QCDvacuum as such expected in nucleon-nucleon collisions. In this regard, the production cross section in these two systems are discussed in the following.

The condition for an inelastic particle production is a large momentum transfer  $Q \gg \Lambda_{\rm QCD}$  between the colliding particles which results in a vanishing running coupling constant  $\alpha_{\rm s}$ . Such scatterings are referred to as hard processes. This context allows to treat hard processes with a formalism based on perturbation theory of the QCD (pQCD), which offers a precise explanation of the underlying physics at high Q.

In the framework of the pQCD, the production cross section in a hard nucleonnucleon collision, for instance a proton-proton collision, can be calculated on the basis of parton-parton scatterings by means of the so-called factorization theorem [Sop97]. For example, consider the following process

$$N + N \longrightarrow h + X \tag{1.3}$$

where N represent the colliding nucleons, h a produced hadron and X other final-state products. The production cross section  $d\sigma_{NN\to h}^{hard}$  of the hadron can be then computed as [SSS09]:

$$d\sigma_{\mathrm{NN}\to\mathrm{h}}^{\mathrm{hard}} = f_{\mathrm{a/N_a}}(x_{\mathrm{a}}, Q^2) \otimes f_{\mathrm{b/N_b}}(x_{\mathrm{b}}, Q^2) \otimes \sigma_{\mathrm{ab}\to\mathrm{c}}^{\mathrm{hard}}(x_{\mathrm{a}}, x_{\mathrm{b}}, Q^2) \otimes D_{\mathrm{c}\to\mathrm{h}}(z, Q^2) \tag{1.4}$$

Here,  $f_{i/N_i}(x_i,Q^2)$  represent the parton distribution function (PDF), which reveals the probability to find a parton of flavor i and momentum fraction  $x_i = p_i/p_{N_i}$  inside the corresponding nucleon. Moreover,  $d\sigma_{ab\to c}^{hard}(x_a,x_b,Q^2)$  describes the perturbative cross section of the partonic scatterig  $a+b\to c+X$ , where an outgoing parton c is produced. Finally,  $D_{c\to h}(z,Q^2)$  corresponds to the fragmentation function (FF), which determines the probability to produce the hadron h from the parton c with a momentum fraction  $z=p_h/p_c$ . The non-perturbative terms of the equation, namely PDF and FF, are obtained experimentally. In Figure 1.5, the production of two sprays of hadrons, known as jets, in a hard hadronic collision is sketched.

In Equation 1.4, it is assumed that a parton-parton interaction  $a + b \rightarrow c + X$  happens in a shorter time frame than previous interactions between partons in

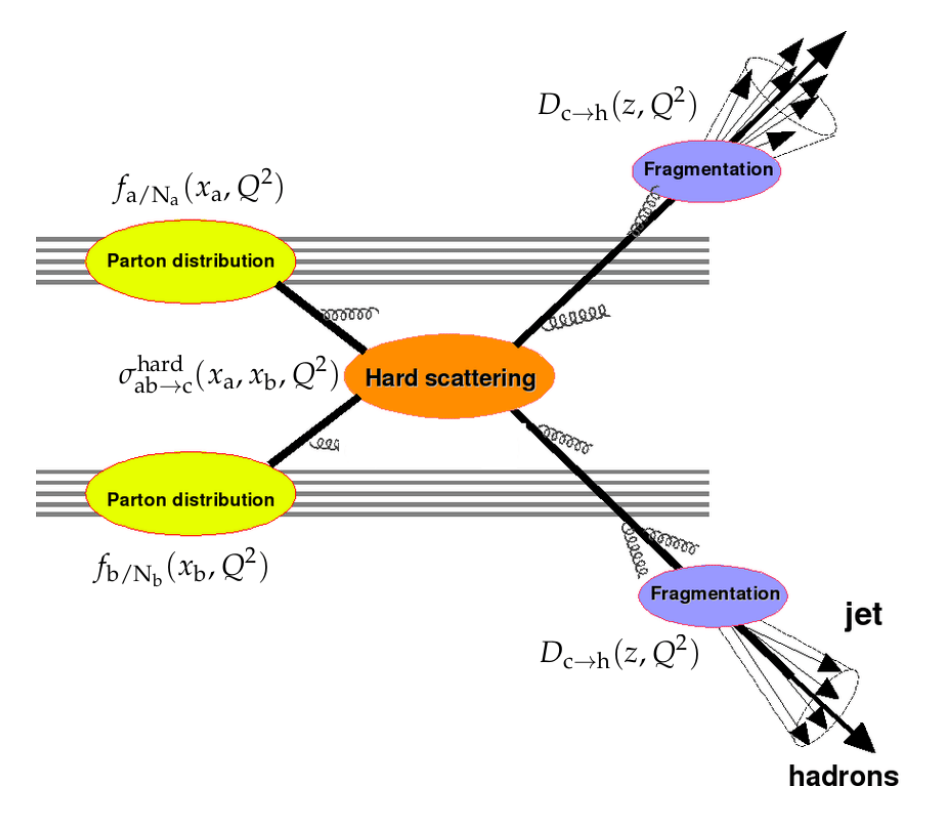


Figure 1.5: Schematic illustration of dijet production and pQCD factorization in a hard hadronic collision. Figure adapted from Figure 6 in [SSS09].

the same PDF or interactions of the outgoing partons c. Effectively this means that the partons appear to be free during the hard interaction. This assumption allows to imagine colliding nuclei as assemblies of free partons. In this picture, the PDF in a nucleus with A number of nucleons can be quantified as [SSS09]:

$$f_{a/A}(x, Q^2) = A \cdot f_{a/N}(x, Q^2)$$
 (1.5)

As a consequence, the production cross section in a nuclei collision (AA) can be then written in terms of the production cross section in a proton-proton collision (pp) scaled  $A^2$  times [SSS09]:

$$d\sigma_{AA}^{hard} = A^2 \cdot d\sigma_{pp}^{hard} \tag{1.6}$$

In experimental high-energy physics, the particle production is measured as invariant yields which leads to [SSS09]:

$$dN_{AA}^{hard}(b) = \langle T_{AA}(b) \rangle \cdot d\sigma_{pp}^{hard}$$
(1.7)

where the nuclear overlap function  $T_{AA}(b)$  characterizes the surface of two colliding nucleon beams as function of the distance b between the beams, also known as impact parameter.

Currently, it is assumed that a QGP can only be created in heavy-ion collisions. This motivates the question of whether an AA collision should be understood in terms of the hadron production as a superposition of pp collisions as proposed in Equation 1.7. Otherwise, the hadron production could be modified due to the presence of a strongly interacting medium. This is usually studied by means of the parton energy loss, which will be discussed in the next section.

#### 1.5 Parton Energy Loss

Jets produced in hard processes are considered extremely useful for the study of the QGP. They originate from partonic interactions at early stages of hard heavyion collisions before the eventual formation of a QGP. This means that they can be directly influenced along their path through the hot medium and, by that, can provide insight on the properties of the QGP. Another prominent feature is that the jet production is well-described in the framework of the pQCD as discussed in the previous section.

Shorty after the theoretical proposition of the QGP, it was suggested by J. D. Bjorken that the influence of the medium could be reflected in a suppression of the jet production resulting from in-medium energy loss of the partons through scattering [Bjo82]. This mechanism is known as "jet quenching". However, note that a suppression of the jet production does not assure the creation of a QGP. In Figure 1.6, a representation of a "jet quenching" in a hard AA collision is shown. In a parton-parton scattering, one parton escapes the medium unaffected and hadronises forming a jet, while the other losses energy by emitting gluons before it fragments into a "quenched" jet.

The total parton energy loss  $\Delta E$  is related with the kinetic properties of the propagating parton, i.e. its initial energy E and mass m, as well as characteristics of the medium, namely the temperature T, the coupling constant  $\alpha_s$  and the thickness L [SSS09]. Moreover, the total energy lost can be split into two mechanisms, namely collisional and radiative energy loss, which are distinguished by the form of scattering they originate from.

Collisional energy loss results from the elastic scattering of partons with the medium constituents and dominates at low particle momenta. The corresponding contribution, shown in [SSS09], has been found to scale linearly with the medium thickness L and logarithmically with the initial parton energy E. For instance, assuming the pass of a charm quark with an initial energy E = 20 GeV through a medium with a temperature T = 0.4 GeV, the lower bound of the energy loss per unit length is 2.3 GeV/fm.

In contrast, radiative energy loss occur with inelastic scatterings of the partons

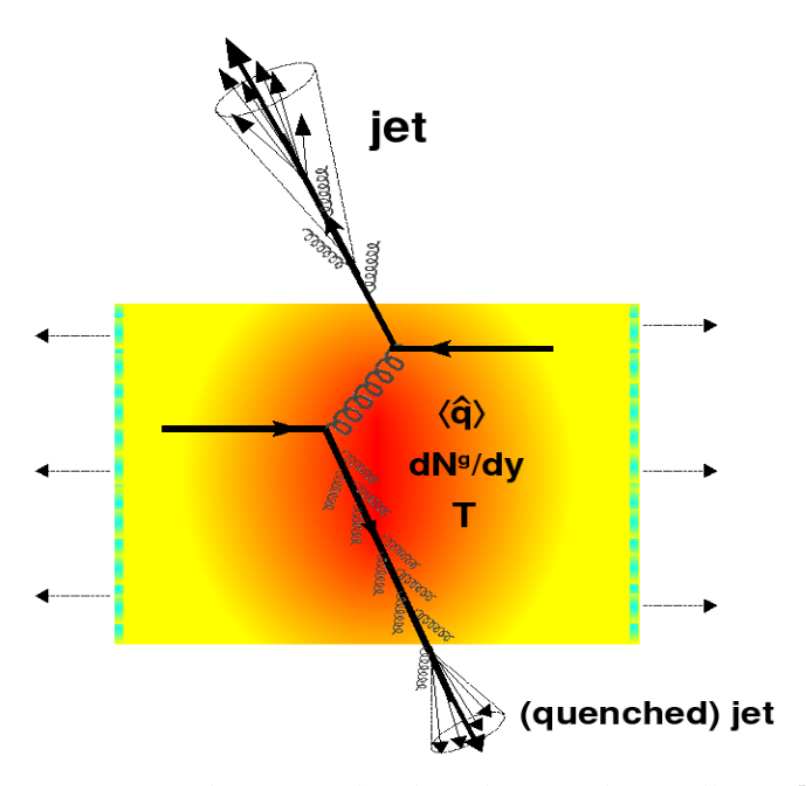


Figure 1.6: "Jet quenching" in a hard nucleus-nucleus collision [SSS09].

with the medium and represents the dominant form of energy loss. The inelastic scattering is produced when a parton traverses the QGP. Subsequently, multiple gluons are radiated due to the influence of the hot medium. The medium-induced modifications are quantified by the so-called transport coefficient parameter  $\hat{q}$ . The radiative energy loss is computed distinguishing between two regimes determined by the medium thickness. Taking as example an initial parton energy E=20 GeV, a thickness L=6 fm and a transport coefficient  $\hat{q}=2$  GeV<sup>2</sup>/fm, the radiative energy loss per unit length is of the order of 10 GeV<sup>2</sup>/fm. It is also worth pointing out, that heavy quarks and the massless partons differ in the scope of the radiation. In certain kinematic regions, the gluon emission from heavy quarks is suppressed leading to an effect called "dead cone". As a consequence, the contribution of collisional energy loss is more relevant for heavy quarks.

# 1.6 Charged-particle Spectra and Nuclear Modification Factors

The suppression of hadron production due to parton energy loss is studied experimentally for different particle species. In this work, the suppression is quantified by comparing the production of non-identified charged particles in heavy-ion collisions, where QGP is potentially created, to the one in pp collisions.

The distributions of charged particles, also called spectra, will be presented in this thesis as function of the pseudorapidity  $\eta$  and the transverse momentum  $p_{\rm T}$  (Appendix A). Possible modifications of the charged-particle production in heavy-ion collisions due to in-medium effects should thus manifest in the corresponding  $p_{\rm T}$  spectra. These modifications are evaluated by means of the so-called nuclear modification factor  $R_{\rm AA}$ , which compares the particle production in AA with the one in pp collisions scaled in accordance to Equation 1.7 via [SSS09]:

$$R_{\rm AA}(p_{\rm T}, \eta, b) = \frac{1}{\langle T_{\rm AA}(b) \rangle} \frac{\mathrm{d}^2 N_{\rm ch}^{\rm AA} / \mathrm{d} \eta \mathrm{d} p_{\rm T}}{\mathrm{d}^2 \sigma_{\rm ch}^{\rm pp} / \mathrm{d} \eta \mathrm{d} p_{\rm T}}$$
(1.8)

Hence, the suppression related with the existence of a QGP will be reflected with a the nuclear modification factor  $R_{\rm AA} < 1$ . In order to prove the validity of measured nuclear modification factors, these can be compared to theoretical models. The model calculations make use of a pQCD factorization of the cross section for hadron production. All of the following models implement different approaches which lead to parton energy loss. Therefore, a comparison of these measurements with the models will help to improve the fundamental understanding of parton energy loss mechanisms. The formalisms of each of the approaches are presented briefly in the following:

- **Bianchi's model [BEK**<sup>+</sup>**17]:** this model describes the production of high  $p_{\rm T}$  hadrons with the fragmentation of hard partons. In a framework based on the hydrodynamics, the energy loss of the parton is characterized by the medium transport coefficient  $\hat{q}$  scaled with the temperature dependent entropy density and the energy scale of jets within the medium.
- CUJET 3.0 [XLG15]: the pQCD formalism provided by its predecessor CUJET 2.0 is upgraded with a description of soft processes by means of a suppression of quark and gluon degrees of freedom and the emergence of chromomagnetic monopoles. The model prediction is calculated by varying the QCD running coupling and the ratio of electric to magnetic screening scales.
- SCET<sub>G</sub>-Vitev's model [CEK<sup>+</sup>16]: this description of inclusive particle production and the suppression consists in the soft-collinear effective theory (SCET) extended with the coupling of Glauber gluons exchanges to the medium. In the calculations, cold nuclear matter effects and parton-to-hadron fragmentation functions are taken into account.
- **Djordjevic's model [DBZ16]:** the energy loss is predicted with pQCD calculations in a dynamical QCD medium of finite spatial extent. In the frame-

work of the  $SCET_G$  model, the prediction discusses the radiative and the collisional energy loss of the partons integrating cold nuclear effects.

In this thesis, the measurement of charged-particle  $p_{\rm T}$  spectra in pp and Pb-Pb collisions collected with the ALICE experiment at CERN and the calculation of the corresponding nuclear modification factors are reported. Finally, the obtained results are compared to the mentioned theoretical models.

# 2 The ALICE Experiment at CERN

The European Organization for Nuclear Research (CERN) was founded in 1954 with the aim of investigating the structure of matter beyond the atomic nuclei and, by that, providing answers to the most fundamental questions about the universe. This research organization is based in Geneva, where it brings together 23 European countries and physicists from all over the globe to collaborate in the study of the nature of fundamental particles. To this end, the organization operates the Large Hadron Collider (LHC), the most powerful accelerator in the world, in order to investigate the particle collisions that take place in it. Several experiments are located along the LHC, the four largest ones being: A Large Ion Collider Experiment (ALICE), A Toroidal LHC Apparatus (ATLAS), Compact Muon Solenoid (CMS) and Large Hadron Collider beauty (LHCb).

The data used in this work was taken with the ALICE experiment, which is dedicated to the study of strong interactions between deconfined quarks and gluons. In this chapter, general aspects of the LHC will be discussed and then a detailed description of the ALICE detectors most relevant for this work is given. In addition, the experimental procedures used for track reconstruction and centrality estimation are briefly explained.

#### 2.1 The LHC

Since the start of its operations in 2008, the LHC has remained the largest and most powerful accelerator ever built. Inside a 27-kilometre underground tunnel, beams of protons and heavy ions are accelerated by the LHC. The collisions systems studied so far at the LHC are proton-proton (pp), proton-lead (p-Pb), lead-lead (Pb-Pb) and xenon-xenon (Xe-Xe). During the first data taking phase of the LHC (2009-2013), it operated at a maximum of  $\sqrt{s}=8$  TeV in pp collisions, which was a record value at the time. After an upgrade of the collider, the maximum centre-of-mass energy was increased to  $\sqrt{s}=13$  TeV in pp collisions during the second data taking phase (2015-2018).

The particle beams are accelerated gradually by the so-called CERN accelerator complex, which is a chain of accelerators and boosters, the LHC being the

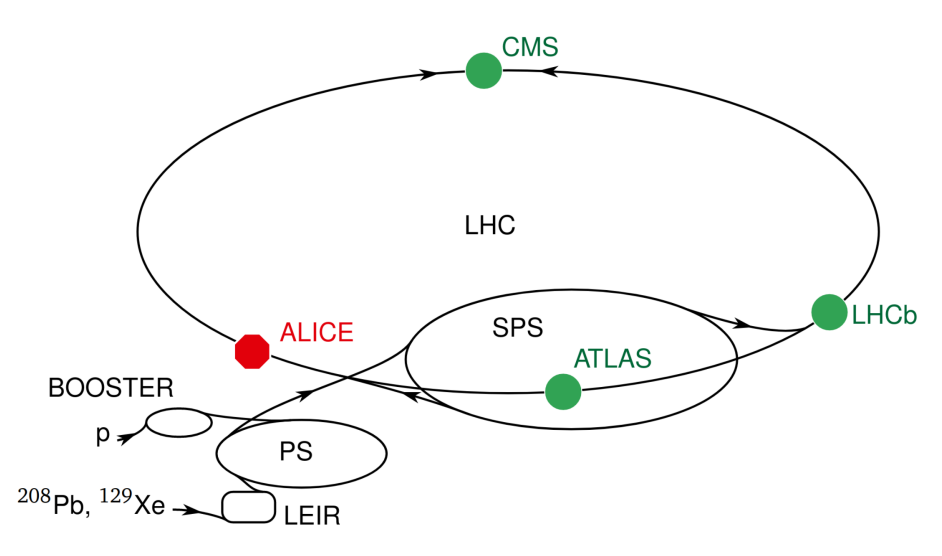


Figure 2.1: Schematic design of the CERN accelerator complex [CERa].

last step of the process. The proton source used for pp collisions is provided through the ionization of hydrogen gas with an electric field. The resulting protons are injected and boosted successively into the Linear accelerator 2 (Linac 2), the Proton Synchrotron Booster (PSB), the Proton Synchrotron (PS) and the Super Proton Synchrotron (SPS). Here, the proton beams reach energies of 450 GeV before they are injected to the beam pipes of the LHC. In the case of lead ions, the source consists of vaporised lead. The lead ions are boosted first in the Linac 3 and the Low Energy Ion Ring (LEIR), before they are injected into the PS. In Figure 2.1, a schematic view of the accelerator complex is shown.

In the LHC, two particle beams are accelerated in opposite directions within two beam pipes at ultrahigh vacuum. A series of superconducting electromagnets produce a magnetic field capable to bend the particle beams through the accelerator. The magnets are connected to a liquid helium supply for cooling purposes. When the particle beams reach ultra-relativistic energies, they are brought to collision inside the four experiments introduced at the beginning of this chapter. This work is based on data measured with the ALICE detectors, which is discussed in detail in the next section.

#### 2.2 ALICE

ALICE is dedicated to the study of strongly interacting matter at temperatures and densities high enough to presumably create a QGP. Hundreds of physicists from 30 different countries participate in the research of this extreme state of matter as part of the ALICE collaboration. The ALICE experiment is located in the vicinity of St Genis-Pouilly in France and lies 54 m under the ground. It is 26 m long, 16 m high and 16 m wide and consists of 18 different detectors installed

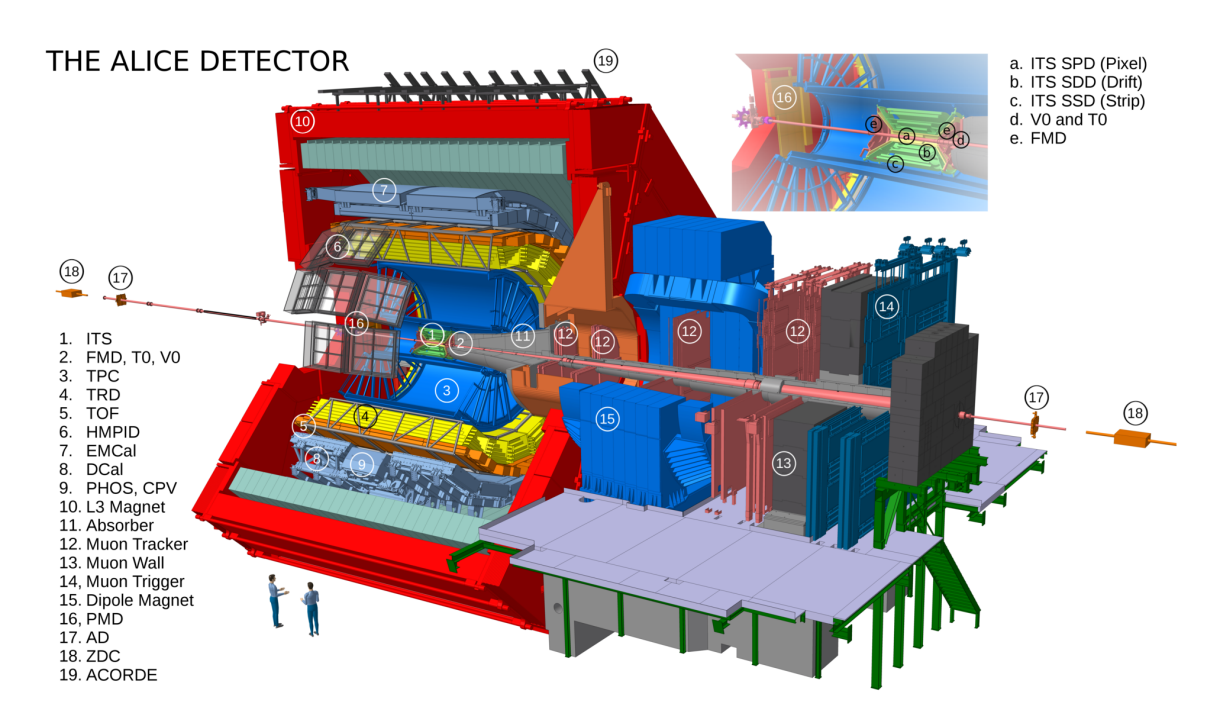


Figure 2.2: Schematic layout of the ALICE detector [Tau17].

in three distinct parts: the central barrel, which is the most relevant part for this work, the forward detectors and the muon spectrometer [BV09].

The central barrel is a cylindric structure built around the beam pipe and installed within the solenoid magnet L3, which produces a magnetic field that bends the trajectory of charged particles. The detectors that form the central barrel are, from the inside out, the Inner Tracking System (ITS), the Time Projection Chamber (TPC), the Time-of-Flight (TOF) detector, the High Momentum Particle Identification Detector (HMPID), the Transition Radiation Detector (TRD) and three electromagnetic calorimeters (EMCAL, DCAL and PHOS). In Figure 2.2, the schematic design of the ALICE experiment is shown.

The forward detectors are located at small angles relative to the beam axis. The two arrays of the V0 detector are placed on both sides of the collision vertex. They are the main trigger detectors and are used to determine the centrality in heavy-ion collisions. Furthermore, the Forward Multiplicity Detector (FMD), next to the V0, and the Photon Multiplicity Detector (PMD), mounted on the L3 magnet door, estimate the multiplicities of charged particles and of photons respectively. Finally, on both ends of the beam pipe the Zero-Degree Calorimeters (ZDC) measure spectator nucleons in heavy-ion collisions.

In this work,  $p_T$  distributions of inclusive charged particles produced in pp collisions as well as in nine Pb-Pb centrality classes are calculated. For this reason, the ITS and the TPC, which are the detectors used for the reconstruction of charged-particles tracks, as well as the V0 detector, required for the centrality estimation, will be discussed in the next sections in more detail.

#### 2.2.1 Inner Tracking System

The ITS is designed to cover a broad number of applications, making it into one of the most important and versatile detectors of the ALICE experiment. The detector is used to reconstruct charged-particle tracks with low momentum and for particle identification. Moreover, the detector is also required for finding the primary vertex and locating of secondary vertices from decays of hyperons and particles carrying heavy flavour.

The ITS is located in the center of the ALICE experiment surrounding the beam pipe. It has a pseudorapidity coverage of  $|\eta| < 0.9$  and an overall radius of 51 cm. It consists of six silicon layers grouped three different subdetector systems with radii between 4 and 43 cm. From the inside out, the subdetectors are the Silicon Pixel Detector (SPD), the Silicon Drift Detector (SDD) and the Silicon Strip Detector (SSD).

At LHC energies, the track density and the radiation near the nominal interaction point reach extreme levels. The SPD, which corresponds to the two innermost layers of the ITS, is designed to measure the collision vertex in such conditions with high precision. In addition, the SPD can also be used for triggering.

The next two layers correspond to the SDD. The layers are able to detect multiple tracks at a time. The SDD is also employed to measure the deposited specific energy loss dE/dx, which is required for the particle identification.

The SSD, which comprises the two outer layers of the ITS, is located near to the TPC in order to match smoothly the track points from the respective detectors. The detector is able to provide tracking points in two dimensions as well as specific energy loss information for the identification of particles with low momentum.

#### 2.2.2 Time Projection Chamber

The TPC is a cylindric detector filled with a gas mixture (Ne-CO<sub>2</sub>-N<sub>2</sub>) and a pseudorapidity coverage of  $|\eta|$  < 0.9 that serves as the main tracking device of charged particles in the ALICE experiment. The main functions of the detector are the three dimensional reconstruction of tracks, the particle identification via specific energy loss and the determination of collision vertices. It has an inner radius of around 0.85 m that surrounds the ITS and an outer radius of around 2.5 m, while the length is approximately 5 m along the beam direction. This corresponds to a detector volume of 88 m<sup>3</sup>. In Figure 2.3, a schematic representation of the ALICE TPC is shown.

When a charged particle traverses the gas mixture of the TPC, electron-ion pairs

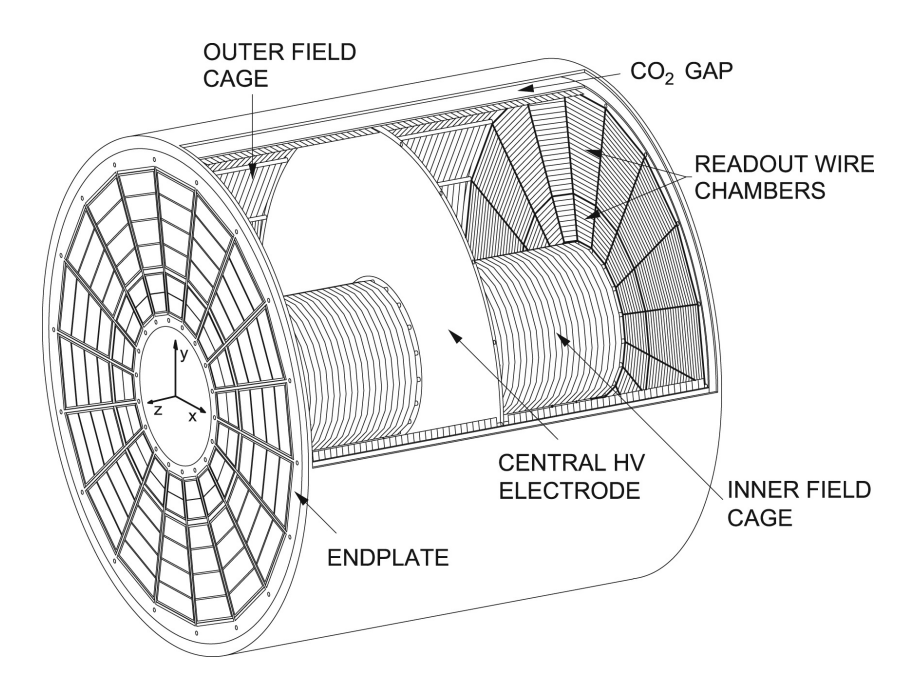


Figure 2.3: Schematic design of the ALICE TPC [AAA+10].

are created through ionization along the track. A uniform electrostatic field is created by means of a central high-voltage electrode and the outer and inner field cages. As a consequence of the electric field, the freed electrons drift towards the readout planes, which are located at the endcaps and which operate as electrodes. Subsequently, two dimensional representation of the track is projected into the readout chambers. The measurement of the drift time of the electron provides due to the constant drift velocity the z coordinate. This allows to reconstruct the particle track in three dimensions. The magnetic field of the L3 magnet, which is parallel to the electric field, bends the trajectory of the tracks such that the momentum of the particle can be calculated by means of the Lorentz force [Wie08].

The two endcaps of the TPC are equipped with multi-wire proportional chambers (MWPC), a type of gas detector, which constitute the readout planes of the TPC. A pad plane at ground potential works as the cathode of the detector which is also used as the outer layer of the MWPC. Above the pad plane, three wire planes form the readout chambers. From the outside in, these are a grid of anode wires at positive high voltage, a cathode wire plane at ground potential and a gating grid. A sketch of a MWPC is given in Figure 2.4.

Between the anode and the cathode, the so-called amplification region is found. Here, the drifted electrons that originated in the TPC volume move under the influence of an electric field which increases with the distance from the anode wires. When the voltage surpasses a certain threshold, electrons carry sufficient energy to ionize atoms, which causes a cascade of more free electrons that in turn ionize more atoms. This leads to an avalanche effect that amplifies the ini-

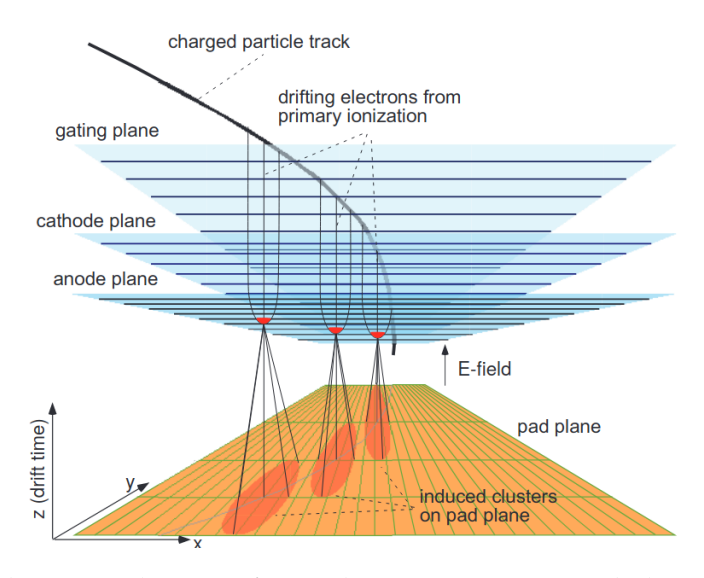


Figure 2.4: Schematic design of a multiwire proportional chamber [Wie08].

tial signal by a factor of  $2x10^4$  [Wie08]. The drift and amplification regions are separated by the gating grid, which has two different modes: open and closed. After an event is triggered and during the drift time that an electron needs over the full TPC length, the gating grid remains open. The open configuration is achieved when all wires of the gating grid have the voltage corresponding to the drift field at the position of the gating grid. Otherwise, it is closed alternating the wires to a positive and negative voltage in order to prevent ions from drifting into the TPC volume and by that causing field distortions [Wie08].

#### 2.2.3 V0 detector

The V0 detector is comprised of two circular arrays of scintillator counters, called V0A and V0C, which are located on both sides of the ALICE interaction point. The V0A array is installed at 3.4 m away from the collision point along the beam direction, while the V0C is placed at 0.9 m away in opposite direction. The arrays cover a rapidity of  $2.8 < \eta < 5.1$  and  $-3.7 < \eta < -1.7$ , respectively. The V0 detector is mainly used to trigger the data taking and to estimate the centrality in heavy-ion collisions. Given the large trigger rate expected from undesired background signal in pp collisions, the V0 detector is designed to discriminate between collision and background events by means of the signal arrival time. For the data used in this work, the signals in both arrays must be in coincidence to fulfill the trigger condition. The procedure used to determine the centrality from the V0 signal will be described at the end of this chapter.

#### 2.2.4 Track reconstruction

The detectors used for the track reconstruction are mainly the ITS and the TPC. The TRD is also used for the tracking of particles with momenta above  $1 \, \text{GeV}/c$ . All detectors involved are specially designed to operate in environments with a high density of tracks. The tracking algorithm can be divided in four phases, namely the merging of signals or clusterization, the identification of a preliminary primary vertex with the SPD, the reconstruction and fitting of the tracks and, finally, the determination of the primary vertex using the information provided by the tracks. In Figure 2.5, a schematic representation of the workflow of the track algorithm is shown.

A charged particle that crosses the set of detectors leave hits in form of cells firing. In the first phase of the track reconstruction, adjacent hits are merged separately in each detector in order to form so-called clusters, which are characterized by several parameters, such as the position, the signal amplitude, the signal time or the corresponding errors. After the clusterization, paths between pairs of clusters, each cluster located in an SPD layer, are determined. The space point where most paths, also called tracklets, converge is designated as the preliminary interaction vertex.

The track finding and fitting occur simultaneously in the framework of the Kalman filter technique [col14]. The reconstruction is performed in three stages, namely first starting in the TPC at large radius and inwards in radial direction, then outwards and, finally, inwards again.

The procedure starts by determining the path through two TPC clusters, beginning with those located at large radii, and the preliminary primary vertex. An analog search is performed using three TPC clusters and without considering the primary vertex. The resulting paths represent the track candidates or seeds. These are propagated inwards to the innermost TPC radii updating the track progressively with the clusters along the way that fulfill a proximity criterion defined by the positions and errors. Next, the tracking continues in the SSD using as starting point the TPC seeds. Analogous to the reconstruction in the TPC in two steps, the seeds are propagated inwards to the SPD updating the seed with clusters at each ITS layer that fulfill the proximity criterion. With this, the first stage of the track finding and fitting concludes.

Tracks with very low momenta are occasionally absorbed by the detector material before entering the TPC, which results in a low reconstruction efficiency in this range. As a result, some TPC tracks can't be connected with ITS clusters. To solve this, tracks in this momentum range are determined in a standalone ITS reconstruction with clusters from the three innermost ITS layers and the prelim-

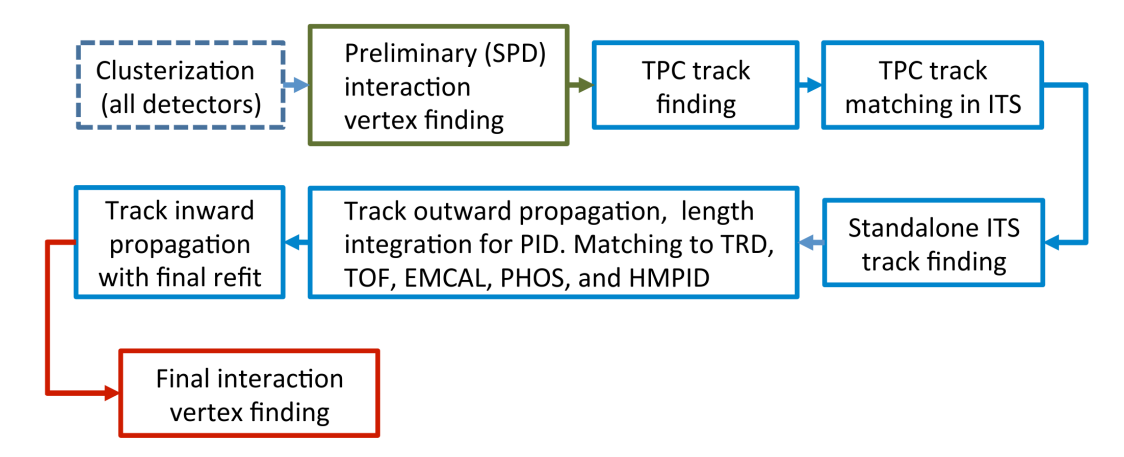


Figure 2.5: Schema of the workflow for the track reconstruction algorithm for charged particles in ALICE. Figure adapted from Fig. 18 in [col14]

inary primary vertex. These seeds are propagated outwards taking into account the proximity cut. Finally, the resulting track candidates are refitted using the Kalman filter.

After the standalone ITS track finding, an extrapolation of all tracks is performed to their point of closest approach to the preliminary primary vertex. Then, the tracks are refitted with the Kalman filter outwards up to the utmost radii of the TPC using the clusters obtained previously. Track parameters are updated at each step for the later particle identification with TOF. The tracks are propagated through the rest of the detectors of the central barrel in an attempt to match them with the tracklets of these detectors. Nevertheless, the propagation beyond the TPC doesn't modify the track parameters, but it is used for particle identification.

In the final step, the resulting tracks are propagated and refitted once again starting from the outer radii of the TPC up to the SPD. In this process, the final track parameters, as for example the inverse of the radius, and the corresponding errors are obtained. Once the reconstruction is completed, the resulting TPC-ITS tracks are used to determine the position of the primary vertex.

#### 2.2.5 Transverse momentum and momentum resolution

The trajectory of a charged particle traveling through the TPC is characterized by a helical form caused by the prevailing magnetic field. This is caused by the Lorentz force which relates the radius r of the track curvature with the transverse momentum  $p_{\rm T}$  of the particle. Thus, the transverse momentum of a track can be calculated via:

$$p_{\rm T} = r \cdot e \cdot B \tag{2.1}$$

where B is the magnetic flux density perpendicular to the particle of charge

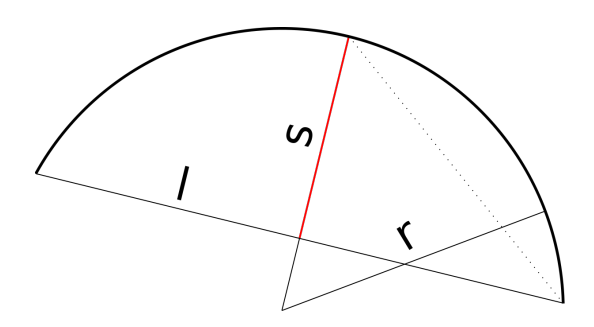


Figure 2.6: Visualisation of the radius r, the sagitta s and the chord l of a circular arc [Wik].

e [Wel]. In practice, the measurement of this radius is demanding since even particles with low transverse momenta present radii that far exceed the outer radius of the TPC. For this reason, the radius is substituted by another quantity which parametrizes the track curvature and can be measured within the detector volume. The used quantity is the so-called sagitta (Figure 2.6), an arc parameter which is inverse proportional to the radius of the track for the extreme case of a chord  $l \ll r$  spanning the base of the arc [Wel]:

$$s = \frac{l^2}{8r} \tag{2.2}$$

Therefore, we obtain for *B* given in Tesla, *l* in m and  $p_T$  in GeV/c [Wel]:

$$s = \frac{0.3e \cdot B \cdot l^2}{8p_{\rm T}} \tag{2.3}$$

The sagitta is measured with an uncertainty due to the spatial resolution of the detectors which in turn implies that the resulting inverse of the transverse momentum is affected by an uncertainty  $\sigma(1/p_T)$ . It can be then shown that the relative transverse momentum resolution  $\sigma(p_T)/p_T$  can be approximated by [col14]

$$\frac{\sigma(p_{\rm T})}{p_{\rm T}} \approx p_{\rm T} \cdot \sigma(1/p_{\rm T}) \tag{2.4}$$

#### 2.2.6 Centrality estimation

The volume of the interaction region in AA collisions depends on the impact parameter b. To characterize the overlap between two nuclei in a collision event, an observable that depends on the impact parameter, namely the centrality, is used. A distinction in centrality classes can be made taking into account the size of the overlap region. Thus, head-on collisions are referred to as central, while those collisions in which nuclei have small overlap are called peripheral. The inbetween centrality classes are denominated semi-central. The centrality is

given as a percentage of the total geometric cross section [AAA<sup>+</sup>13].

In this context, nucleons of colliding nuclei are classified in participants or spectators depending on whether they take part in the collision or not. The number of participants  $N_{part}$  in a collision is connected to the number of binary collisions  $N_{\text{coll}}$ . The relation between these geometrical quantities with the impact parameter is described by the so-called Glauber Model [MRSS07], in which colliding nuclear are presented as a superposition of binary nucleon-nucleon collisions. The nucleon density distribution is assumed to follow a Woods-Saxon distribution. The model also makes use of another observable, which quantifies the number of ancestors  $N_{\text{ancestors}}$  in a collision, i.e. emitters of particles. This quantity is calculated with  $N_{\text{ancestors}} = f \cdot N_{\text{part}} + (1 - f) \cdot N_{\text{coll}}$ , where f represents a free parameter. This is based on two-component model, which assumes that soft processes are responsible for the production of an average multiplicity proportional to  $N_{\text{part}}$ , while hard processes scale with increasing  $N_{\text{coll}}$ . Since none of these observables can be measured experimentally, the estimation of the centrality must be based on a measurable quantity, namely the charged-particle multiplicity  $N_{\rm ch}$ . Given that the particle production scales with the number of interactions, the multiplicity is expected to increase with the centrality. Thus, centrality classes are connected to multiplicity classes.

In this context, it should be mentioned that the measured  $N_{\rm ch}$  distribution in peripheral collisions, which are related to low multiplicities, is biased due to inaccuracies in the triggering. This region of the distribution is also affected by events from electromagnetic interactions due to the high cross section of these processes in peripheral collisions at LHC energies. To describe the unbiased low multiplicity region of the  $N_{\rm ch}$  distribution, a parametrization with a negative binomial distribution (NBD) is performed. Here, the assumption is made that the particle production in nucleon-nucleon interactions occurring in AA collisions can be reproduced using as baseline the production in pp collisions [Por19]. To this end, the multiplicity in nucleon-nucleon interactions is predicted with a Monte Carlo (MC) simulation on the basis of an  $N_{\rm ch}$  distribution in pp collisions, which is well described by a negative binomial distribution. The NBD provides the probability  $P_{\mu,k}(n)$  for the production of n particles per ancestor, where  $\mu$  is the mean multiplicity per ancestor and k parametrizes the width of the  $N_{\rm ch}$  distribution.

In the framework of the Glauber Monte Carlo, AA collision events are simulated. From the corresponding geometries,  $N_{\rm part}$  and  $N_{\rm coll}$  values are inferred for each event, which in turn leads to the determination of  $N_{\rm ancestors}$ . Next, the  $N_{\rm ch}$  distribution in pp collisions provided by an NBD is sampled  $N_{\rm ancestors}$  times in order to obtain the  $N_{\rm ch}$  of the simulated AA event. Here, the NBD is optimized to

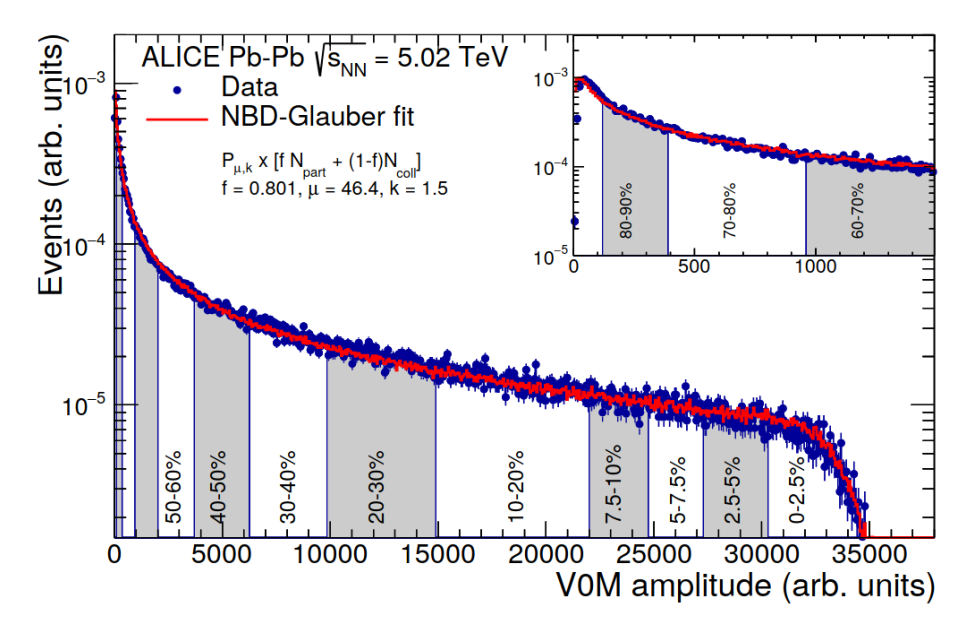


Figure 2.7: Multiplicity distribution measured with the V0M array and parametrized with a NBD-Glauber fit. Centrality percentiles are also represented [AAA<sup>+</sup>13].

minimize the  $\chi^2$  of the fit by adjusting the parameters  $\mu$ , k and f. The sum of the resulting  $N_{\rm ch}$  in each event leads to a prediction of the unbiased  $N_{\rm ch}$  distribution in AA collisions.

Figure 2.7 shows as example the  $N_{\rm ch}$  distribution in Pb-Pb collisions at a center-of-mass energy  $\sqrt{s_{\rm NN}}=5.02$  TeV. The distribution is measured with the deposited energy in the V0M array. This is compared to the prediction made by the NBD-Glauber fit. The distribution presents a peak that corresponds to the peripheral collisions, while the plateau covers the region of semi-central collisions and the edge the interval of central collisions. As expected, the NBD fit is in good agreement with data at mid and high multiplicities, but not at low multiplicities. In the figure, the centrality classes are also given. These are determined by defining an upper bound for the range in which the measurement is not biased. The estimation of the centrality classes is anchored to this upper bound, also called anchor point, which in case of ALICE is established at 90 %. Below the anchor point, the centrality classes are derived from the integral of the measured distribution, while above it the NBD parametrization is used.

# 3 Analysis

As discussed in the first chapter of this work, the physics of strongly interacting matter can be investigated by means of the nuclear modification factor  $R_{\rm AA}$  which compares the yield of inclusive charged particles in AA collisions and a corresponding reference measurement in pp collisions. In this chapter, an analysis of transverse-momentum distributions in Pb-Pb and in pp collisions at a center-of-mass energy  $\sqrt{s_{\rm NN}}=5.02$  TeV measured with ALICE is presented. First, the selected data samples are detailed. Then, the procedures to correct for detector effects which have an impact on the  $p_{\rm T}$  distributions are described. With these corrected  $p_{\rm T}$  distributions the nuclear modification factors are calculated. The results are discussed and compared to previous ALICE measurements reported in [AAA+18].

#### 3.1 Data sample

This thesis is making use of pp and Pb-Pb collisions at  $\sqrt{s_{\rm NN}}=5.02$  TeV recorded by ALICE in the years 2017 and 2018 respectively. For the pp data takings, the interaction rate was 50 kHz, while in Pb-Pb it was 7.5 kHz. Furthermore, the ALICE collaboration provides for each data taking period at least one Monte Carlo (MC) production, which simulates the exact same conditions and technical specifications of the detector at the time of data taking, anchored to it. The particle collisions for the MC productions were generated by PYTHIA [SMS08] in the case of pp collisions and by HIJING [WG91] for the Pb-Pb collisions, while the corresponding detector response was simulated by GEANT3 [GEA]. The limited computing time available for these simulations allows to cover only a percentage of the total statistics present in data. An overview of the number of events contained in each data set is summarized in Table 3.1. The number of events was measured after the event selection depicted in the following section of this chapter.

The examined pp data consists of two separate subsets that differ by their readout configuration: the first data subset corresponds to collisions measured excluding the detector signal of the SDD layers, which in this thesis will be referred

System	statistics (M)	MC generator	MC statistics
	560 (FAST)		
pp		PYTHIA + GEANT3	25 %
	318 (CENT)		
Pb-Pb	110	HIJING + GEANT3	2 %

Table 3.1: Overview of the analyzed collision systems, the approximate number of events and the MC productions, they are associated with, including the percentage of simulated statistics [Groa].

to as *FAST* in accordance with ALICE convention. The exclusion of the signal occurs whenever the SDD is inoperable due to its dead time. In contrast, the collisions in the second data subset were reconstructed including the information of the SDD layers. These collisions are labeled as *CENT*.

As shown in Table 3.1, the *FAST* subset contains significantly more events than *CENT*. In this work, these two data takings are combined in order to make use of all measured pp collisions. In the big picture, this increase of statistics will lead to an enhanced precision in the high  $p_T$  region and to an enlarged  $p_T$  reach of the charged-particle  $p_T$  spectrum in pp collisions. Such an improvement will in turn be reflected in the nuclear modification factors.

#### 3.2 Trigger and event selection

#### 3.2.1 Trigger

During the data taking, a trigger decides in real time whether a collision candidate is worth to be stored or not. The ALICE experiment focuses its research activities on the investigation of strongly interacting matter and therefore inelastic collisions are of particular interest. Moreover, the trigger is also designed to reject undesired beam-gas interactions.

The trigger configuration which imposes the smallest bias and thus accepts the majority of the overall inelastic cross section is called minimum bias (MB) trigger. For the data sets used in this thesis, a MB trigger ( $V0_{and}$ ) that requires signals both in the V0A and V0C detectors in coincidence with the bunch crossing is used [col14].

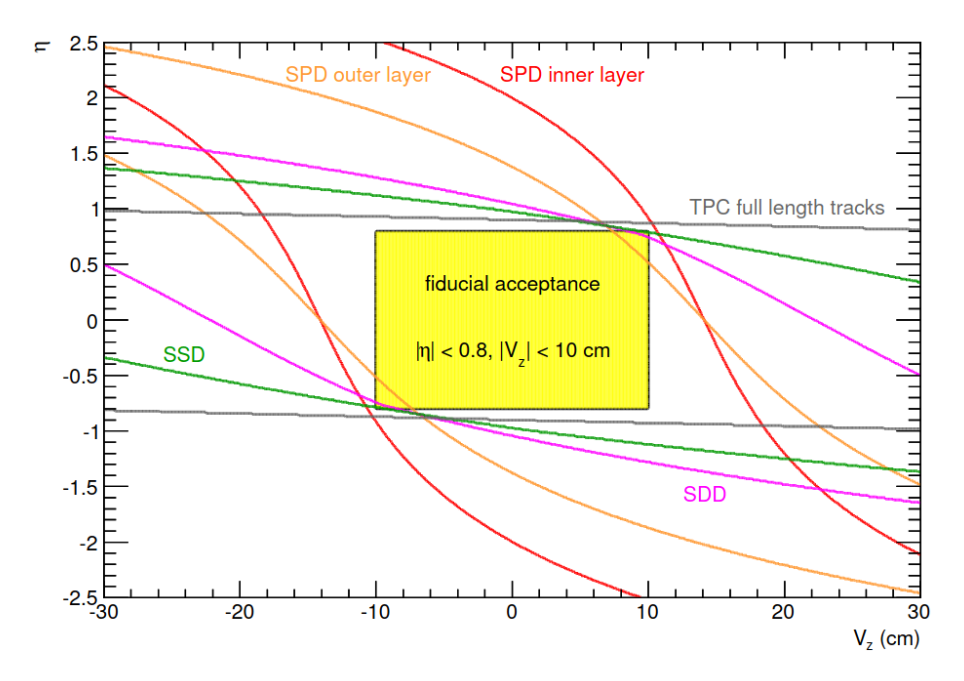


Figure 3.1: Pseudorapidity acceptance of the SPD, the SDD, the SSD and the TPC shown as function of the position of the primary vertex along the *z*-axis. The fiducial acceptance represents the region where most tracks can be reconstructed [Kni14].

#### 3.2.2 Selection of events

In an offline stage of the event selection, collision candidates that satisfy the trigger condition undergo a selection process in order to reduce the contamination with poor quality events. A part of this contamination corresponds to a background signal originated from interactions of the beams with the machine. This beam background originates upstream of the V0 modules. The arrival time of background events is thus shorter than the one of a collision produced in the nominal interaction point. This difference is exploited to exclude background events from the data sample [col14]. Another source of contamination are the so-called pile-up events, which are events produced in a bunch crossing different from the one that triggered the data recording. In addition, multiple collisions occurring within the same bunch crossing are also considered pile-up, although this takes place much more rarely.

The pseudorapidity acceptance of the ALICE tracking detectors depends on the position of the primary vertex  $V_z$  along the beam axis z as illustrated in Figure 3.1 for the ITS subdetectors and the TPC. To ensure a symmetric pseudorapidity coverage of  $|\eta| < 0.8$ , the vertex position was restricted to  $|V_z| < 10$  cm.

Track variable	Condition			
Selection of primaries				
$DCA_z$	≤ 2 cm			
$DCA_{xy}$	$\leq 7\sigma$			
ITS selection				
at least one hit in the SPD	required			
ITS refit	required			
$\chi^2$ per ITS cluster	< 36			
TPC selection				
TPC refit	required			
$\chi^2$ per TPC cluster (pp collisions)	< 4			
$\chi^2$ per TPC cluster (Pb-Pb collisions)	< 2.5			
fraction of shared TPC clusters	< 0.4			
ratio of crossed rows over findable clusters	> 0.8			
geometric length (TPC dead zone)	3 cm			
geometric length (track length)	130 cm			
TPC-ITS selection				
$\chi^2$ TPC constrained track vs. global track	≤ 36			

Table 3.2: Standard track selection criteria used for analysis of primary charged particles in ALICE.

#### 3.3 Track selection

In this work, charged particles with a mean proper lifetime larger than 1 cm/c, which originate directly from the collision event or from decays of particles with a lifetime smaller than 1 cm/c, are studied [Col17]. Charged particles that meet these requirements are called primary particles, while those that don't are referred to as secondary particles. The following particle types are considered primary particles: pions  $\pi^+$ , kaons  $K^+$ , protons p, the sigma baryons  $\Sigma^+$  and  $\Sigma^-$ , electrons  $e^-$ , muons  $\mu^-$ , xi baryons  $\Xi^-$  and omega baryon  $\Omega^-$  as well as the respective antiparticles.

Charged particles traverse the TPC-ITS detector system describing a trajectory or

track which can be reconstructed by means of the procedure detailed in Section 2.2.4. These tracks must fulfill several requirements which aim to select good resolution tracks and reduce the contamination from secondary particles present in the data sample. Over the years, the track selection criteria or track cuts have been refined by several analyses on the charged-particle production in ALICE, such as [Kni14], [PL18] and [Gro18]. As a result, the standard track selection listed in Table 3.2 was established. Here, the same track cuts are implemented in both collision systems pp and Pb-Pb for tracks measured in the kinematic range  $p_{\rm T} > 0.15~{\rm GeV}/c$  and  $|\eta| < 0.8$ , in data as well as in in the corresponding MC productions.

#### 3.4 Corrections

After implementing the event and track selections, the uncorrected  $p_T$  dependent distributions of the produced charged particles in pp and Pb-Pb collisions can be calculated as shown in Figure 3.2. In the case of heavy-ion collisions, the  $p_T$  distributions are divided into nine centrality classes. The vertical error bars represent the statistical uncertainties.

These  $p_T$  distributions are influenced by several detector effects that must be corrected for. To this end, most of the corrections are implemented using information provided by MC simulations. In addition, data-driven approaches are used to correct for imperfections of these simulations.

Two groups of corrections can be defined according to the level at which they operate, namely event-level corrections, which affect the overall normalization of the spectrum, and track-level corrections, which are  $p_{\rm T}$  dependent and condition consequently the shape of the spectrum. The corrections applied in this thesis are listed below.

- Overall normalization (Section 3.4.1): The  $p_{\rm T}$  distributions must be normalized by the total number of inelastic events  $N_{\rm INEL}$ . Some inelastic events aren't triggered or their vertex is missing. The number of reconstructed events  $N_{\rm ev}^{\rm rec}$  corresponds thus to a fraction of  $N_{\rm INEL}$ . The trigger and vertex reconstruction efficiencies must be therefore determined and  $N_{\rm ev}^{\rm rec}$  correspondingly corrected.
- **Signal loss (Section 3.4.2):** As a consequence of the trigger and vertex reconstruction efficiencies, tracks from missing events aren't reflected in the raw  $p_T$  distributions. To take them into account, the signal loss is calculated using the information provided by MC simulations.

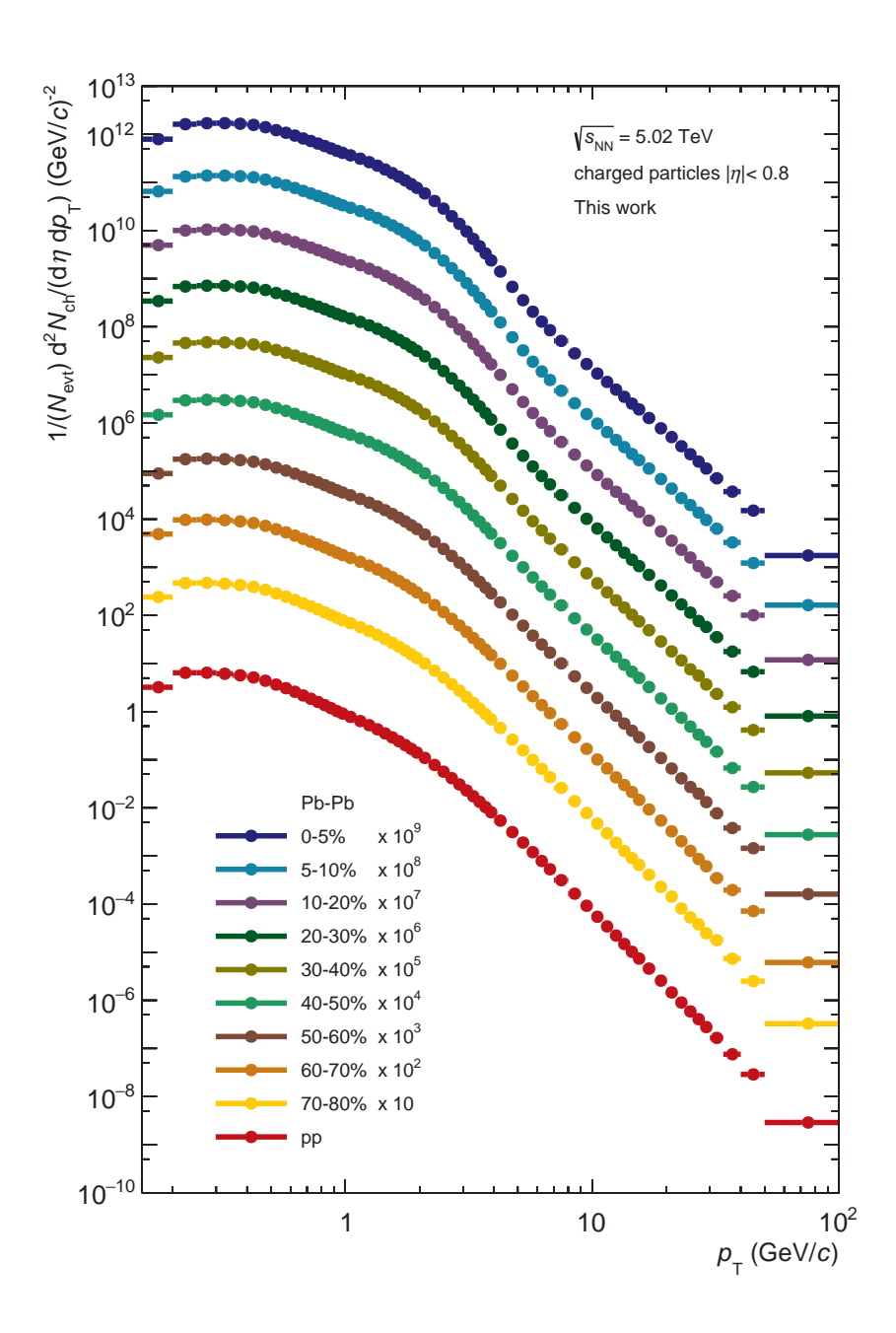


Figure 3.2: Uncorrected transverse-momentum distributions of primary charged particles produced in pp and Pb-Pb collisions at  $\sqrt{s_{\rm NN}} = 5.02$  TeV. The latter are divided into nine centrality classes. The  $p_{\rm T}$  spectra of Pb-Pb collisions are scaled with a logarithmic factor for a better visibility.

• Tracking efficiency and acceptance (Section 3.4.3): Tracks are measured by the TPC-ITS system with a  $p_{\rm T}$ -dependent probability, which results from the existence of a tracking efficiency and the geometrical acceptance. The overall efficiency can be calculated using MC information. Furthermore, it should be noted that the overall efficiency depends on the particle type. Since MC event generators underestimate the production of strange par-

ticles, the overall efficiency must be corrected by reweitghing it with the relative abundance of each particle type. This thesis makes use of the reweighing factors determined in [Huh17], which correct for this effect.

- Contamination by secondary particles (Section 3.4.4): A small amount of secondary particles remain in the measured track sample despite the track selection criteria. This contamination is estimated using MC information. Moreover, the contamination must be corrected for the above-mentioned underestimation of strange particles, which represent a significant fraction of the contamination. This is carried out by scaling the contamination with correction factors obtained in a data-driven approach which exploits the differences between the  $DCA_{xy}$  distributions of primaries and secondaries.
- Transverse momentum resolution (Section 3.4.5): The  $p_{\rm T}$  resolution (see Equation 2.4) results in a smearing of the raw  $p_{\rm T}$  distributions, specially in the high  $p_{\rm T}$  region given the steeply falling shape. A  $p_{\rm T}$ -dependent correction factor is extracted in a toy MC simulation from the ratio of an approximation of the true  $p_{\rm T}$  distribution, corresponding in this thesis to the results of the previous ALICE measurement of  $R_{\rm AA}$  [AAA<sup>+</sup>18], to a  $p_{\rm T}$  distribution affected by smearing caused by the  $p_{\rm T}$  resolution.

In the following sections, the source of the effects that distort the  $p_T$  distributions as well as the mentioned corrections will be discussed in detail.

#### 3.4.1 Overall normalization

The total number of inelastic events  $N_{\rm INEL}$  is used to normalize the  $p_{\rm T}$  distributions. The number of inelastic events  $N_{\rm ev}^{\rm rec}$  that passed the selection criteria doesn't include some events that were not triggered on or reconstructed. These two phenomena are corrected for by means of the so-called trigger efficiency  $\epsilon_{\rm Trig}$  and the vertex reconstruction efficiency  $\epsilon_{\rm Vz}$ :

$$N_{\rm INEL} = \frac{N_{\rm ev}^{\rm rec}}{\epsilon_{\rm Trig} \cdot \epsilon_{\rm Vz}} \tag{3.1}$$

In heavy-ion collisions, both trigger and vertex reconstruction efficiency have been observed to be unity in the studied centrality interval of 0-80 % [AAA<sup>+</sup>18]. However, the bias has a notable influence in pp collisions. The determination of the respective efficiencies in pp collisions is described below.

#### Trigger efficiency

The MB condition of the ALICE trigger system is able to measure a significant percentage of the total inelastic cross section, yet this measurement is limited due to the efficiency  $\epsilon_{\text{Trig}}$  of the trigger. This efficiency connects the inelastic cross section  $\sigma_{\text{vis}}$  seen by the ALICE detector system and the total inelastic cross section as follows  $\sigma_{\text{INEL}}$ :

$$\epsilon_{\text{Trig}} = \frac{\sigma_{\text{vis}}}{\sigma_{\text{INEL}}}$$
 (3.2)

For each data taking period, the visible cross section is measured by determining the luminosity of the experiment, a quantity that evaluates the number of particle collisions in a given period of time to the cross section. For this purpose, a technique called van-der-Meer scan is used, in which the two particle beams are displaced with respect to each other in the transverse directions and the rate of interactions is monitored as a function of this displacement. The ratio of the head-on rate to the luminosity then corresponds to the visible cross section [vdM68]. In the studied pp collisions collected in 2017 at  $\sqrt{s} = 5.02$  TeV, the visible cross section amounts to  $\sigma_{\rm vis} = 50.87 \pm 1.07$  mb [Grob].

The total inelastic cross section  $\sigma_{\rm INEL}$  has not been measured in pp collisions at  $\sqrt{s}=5.02$  TeV. However, a Monte Carlo Glauber model is able to predict it by means of a data-driven parametrization the value of  $\sigma_{\rm INEL}$  as function of the center-of-mass energy [LKd18]. Here, experimental values from several collaborations are utilized as input. According to the prediction, the total inelastic cross section at  $\sqrt{s}=5.02$  TeV is  $\sigma_{\rm INEL}=67.6\pm0.6$  mb [LKd18]. The resulting trigger efficiency is 75.25 %.

#### Vertex reconstruction efficiency

The vertex reconstruction efficiency  $\epsilon_{Vz}$  can be defined as follows:

$$\epsilon_{\rm Vz} = \frac{N_{\rm Vtx}}{N_{\rm Trig}}$$
 (3.3)

where  $N_{\text{Vtx}}$  is the number of events for which a vertex was reconstructed and  $N_{\text{Trig}}$  is the total number of triggered events. Both values are determined before the event selection. The resulting efficiency is 96.67 %.

### 3.4.2 Signal loss

A fraction of the inelastic events is missing due to the trigger and vertex reconstruction efficiency. In order to determine the tracks from missing events, a correction at track-level is required. This is achieved using the MC production

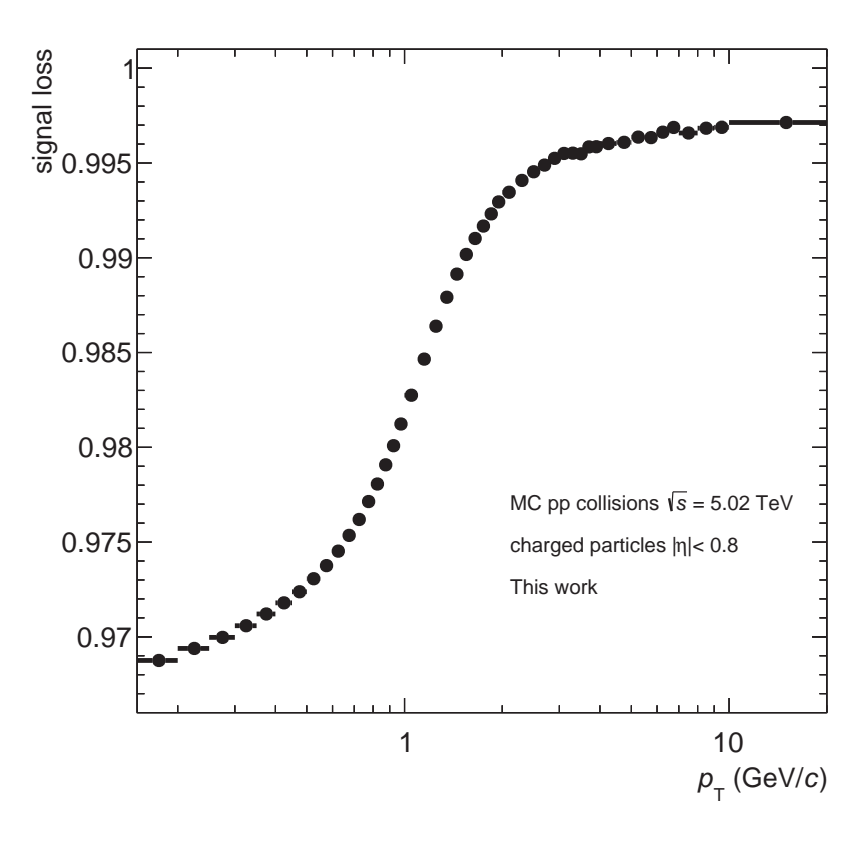


Figure 3.3: Signal loss as function of the transverse momentum for pp collisions.

to compare the distribution of primary tracks generated from inelastic events within the vertex cut  $|V_z|$  < 10 cm before and after they undergo the event selection:

$$\chi_{\text{s.l.}}(p_{\text{T}}) = \frac{(\text{d}N/\text{d}p_{\text{T}})_{\text{Generated}}^{\text{After event selection}}}{(\text{d}N/\text{d}p_{\text{T}})_{\text{Generated}}^{\text{True INEL, }|\text{Vz}|<10 \text{ cm}}}$$
(3.4)

As a result, the  $p_T$  dependent distribution of the signal loss  $\chi_{s.l.}(p_T)$  is shown in Figure 3.3. The effect is more pronounced at low  $p_T$ , where it amounts to about 3 %. The signal loss decreases, becoming negligible above  $p_T = 10 \text{ GeV}/c$ . The required correction is implemented by scaling the  $p_T$  spectrum in each  $p_T$  interval with the inverse of the corresponding value of the signal loss.

## 3.4.3 Tracking efficiency and acceptance

The TPC-ITS detector system is able to measure most of the tracks that cross the detector volume. However, the reconstruction algorithm is sometimes unable to detect a track or to reconstruct it correctly which as a consequence results in its discard due to the track selection. Limitations of the geometrical acceptance can affect likewise the track reconstruction and they should be therefore also taken into account.

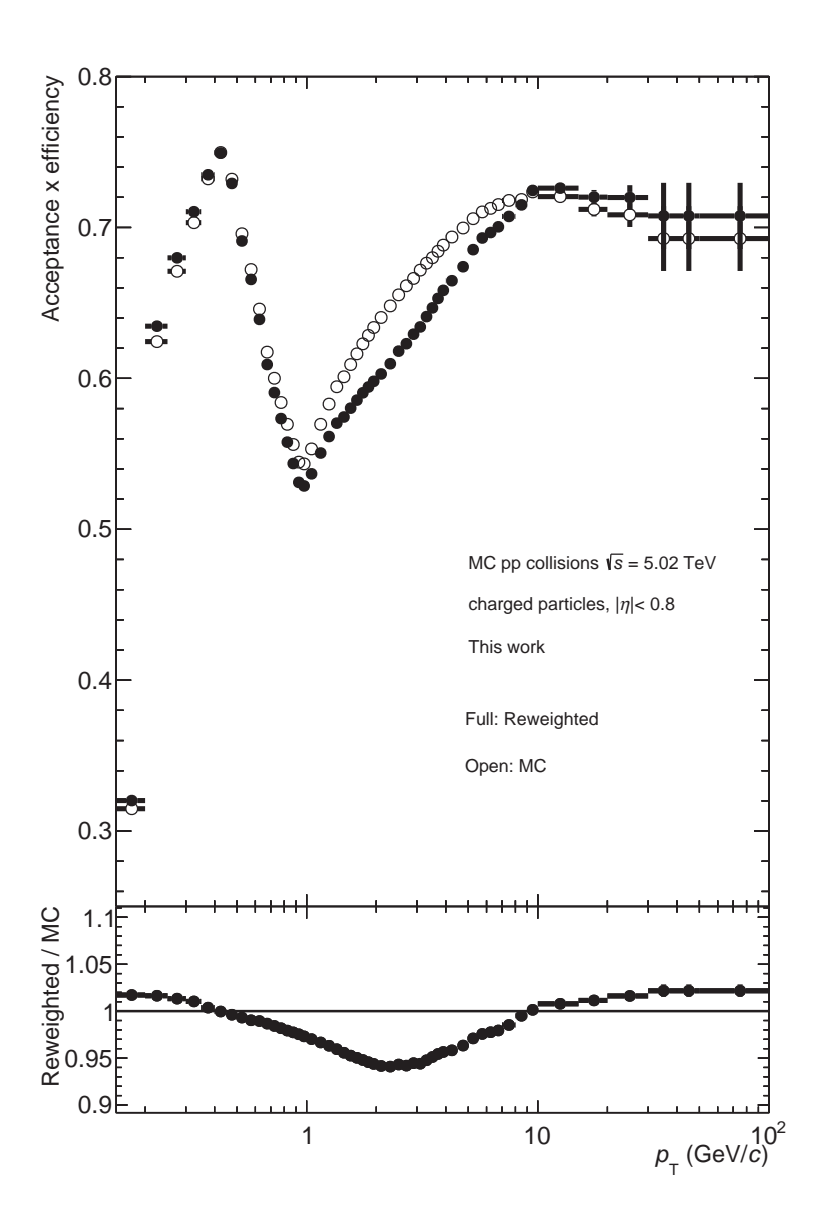


Figure 3.4: Acceptance and tracking efficiency as function of the transverse momentum for pp collisions determined with MC simulations. The overall efficiencies obtained before and after the reweighting are represented with open and full markers, respectively.

The tracking efficiency and acceptance can be summarized in an overall detection efficiency  $\epsilon$  for the reconstruction of tracks which depends on the transverse momentum  $p_T$ . The implementation of the corresponding correction will thus affect the shape of the  $p_T$  distributions. The  $p_T$  dependent efficiency is calculated using the MC simulations as the ratio of reconstructed primary charged-particle tracks that survive the track selection  $N_{\text{prim,rec}}^{\text{MC}}$  to generated primary charged

Centrality class	Scaling factor	
0-5 %	0.980	
5-10 %	0.989	
10-20 %	1.000	
20-30 %	1.010	
30-40 %	1.014	
40-50 %	1.018	
50-60 %	1.021	
60-70 %	1.023	
70-80 %	1.024	

Table 3.3: Scaling factors obtained from the parametrization of the ratios in Figure 3.5.

particles  $N_{\text{prim,gen}}^{\text{MC}}$ :

$$\epsilon(p_{\rm T}) = \frac{N_{\rm prim,rec}^{\rm MC}(p_{\rm T})}{N_{\rm prim,gen}^{\rm MC}(p_{\rm T})}$$
(3.5)

For the correction, the inverse of the overall efficiency is applied as a multiplicative factor in each  $p_T$  interval of the  $p_T$  spectra.

The overall efficiency also depends on the particle type. This requires a complementary correction, explained later on, which scales the overall efficiency by means of the relative abundance of each particle species [Huh17].

In Figure 3.4, the overall efficiency as function of  $p_{\rm T}$  is shown for pp collisions. Here, the efficiency amounts to a value between 54 % and 75 % over the entire  $p_{\rm T}$  range. At low  $p_{\rm T}$ , below 0.4 GeV/c, there is a rapid growth of the efficiency which can be explained by the increasing radii of the particle trajectories making it more likely for the track to fulfill the strict selection criteria. After reaching the maximum, the curve drops quickly and hits its minimum around  $p_{\rm T}=1~{\rm GeV}/c$ . This slump is caused mainly by the track length cut listed in Table 3.2 which aims for a selection of tracks that fulfill a minimal geometric length within the fiducial detector volume. The tracks in the  $p_{\rm T}$ -range of the slump tend to cross the TPC boundaries so that they are less likely to be selected. Following this, the distribution increases asymptotically due to the acceptance restrictions of the detector up to reaching a plateau. At even higher  $p_{\rm T}$ , the trend hints at a declining efficiency. Nevertheless, the overall efficiency is assumed to be constant for  $p_{\rm T} \geq 40~{\rm GeV}/c$  in order to reduce statistical fluctuations. This same trend

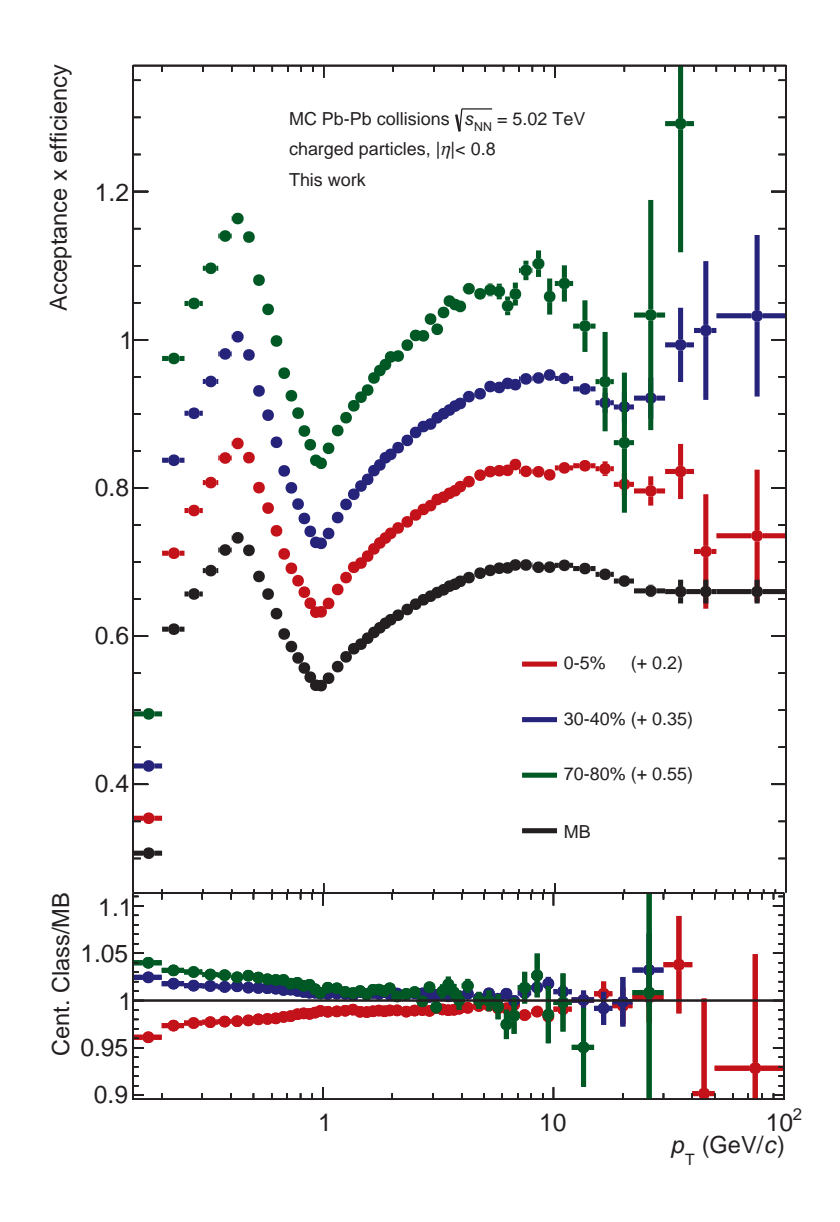


Figure 3.5: Tracking efficiency as function of the transverse momentum for MB, central, semi-central and peripheral Pb-Pb collisions obtained from MC simulations. An offset value is added to the efficiencies for better visibility. In the bottom panel, the ratio of the individual efficiencies to the MB efficiency is shown.

of the efficiency is also observed for the Pb-Pb collisions analysed in this thesis as illustrated in Figure 3.5, which shows the efficiency as function of  $p_{\rm T}$  for MB, central (0 – 5 %), semi-central (30 – 40 %) and peripheral (70 – 80 %) collisions. Here, it is observed that the efficiency decreases with centrality. Towards peripheral collisions, the high  $p_{\rm T}$  range of the centrality-dependent efficiencies is dominated by increasing statistical fluctuations. To avoid the propagation of these fluctuations to the corrected  $p_{\rm T}$  spectra, the ratios of the individual effi-

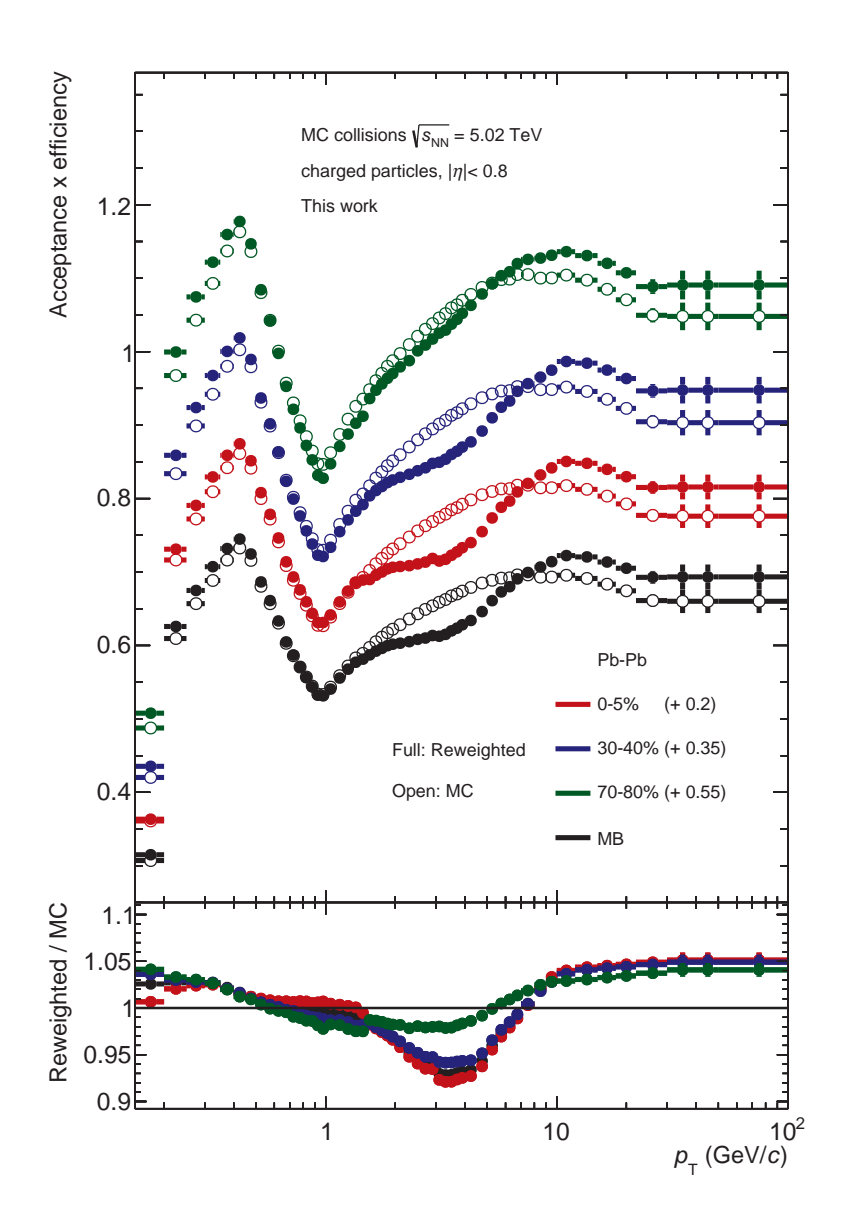
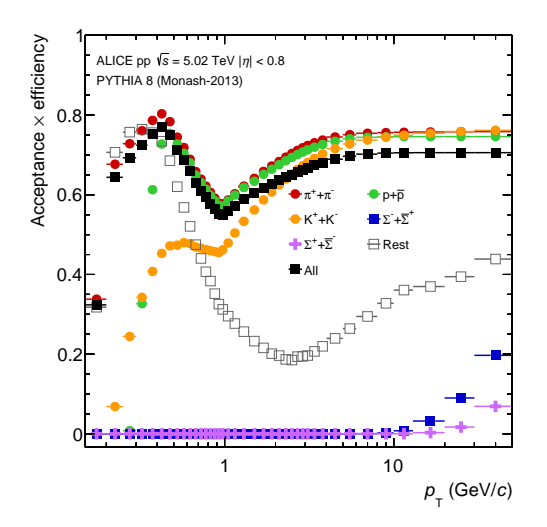


Figure 3.6: Tracking efficiency as function of the transverse momentum for MB, central, semi-central and peripheral Pb-Pb collisions obtained from the scaling of the distributions in Figure 3.5 using the values listed in Table 3.3. The overall efficiencies obtained before and after the reweighting are represented with open and full markers, respectively. An offset value is added to the efficiencies for a better visibility.

ciencies to the MB efficiency, illustrated in the bottom panel, are parametrized in the range  $1.5~{\rm GeV}/c \le p_{\rm T} \le 10~{\rm GeV}/c$  with a constant function. The obtained factors, summarized in Table 3.3, are used to scale the MB tracking efficiency for  $p_{\rm T} > 1.5~{\rm GeV}/c$ , while the original efficiencies are used below this range. As a result, the distributions obtained using this approach are represented in Figure 3.6 with full markers.



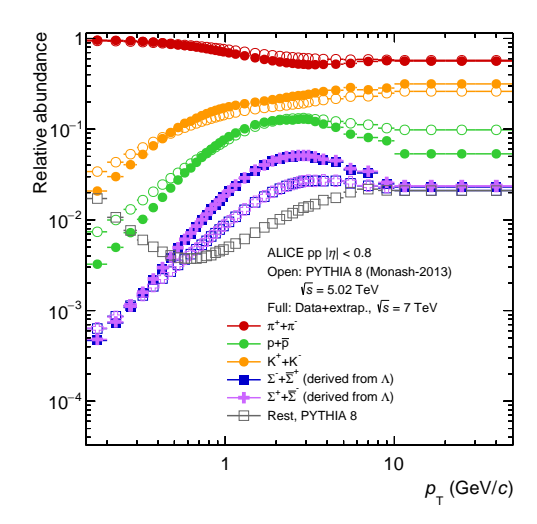


Figure 3.7: **Left:** Tracking efficiencies as function of the transverse momentum for different particle species obtained with a PYTHIA (Monash 13) simulation of pp collisions at  $\sqrt{s} = 5.02$  TeV. **Right:** Relative particle abundances as function of the transverse momentum in data (full symbols,  $\sqrt{s} = 7$  TeV) and in MC (open symbols,  $\sqrt{s} = 5.02$  TeV) [AAA<sup>+</sup>18].

#### Particle composition correction

Primary charged particles present a wide disparity in terms of lifetime. For instance, the pions  $(\pi^{\pm})$ , the most frequent particle type produced in particle collisions, can travel on average 7.8 m within their lifetime, whereas the sigma baryons  $(\Sigma^{\pm})$  have a decay length of only 2.4 cm  $[T^{+}18]$ . As a consequence, some particles are more likely to be rejected by the track length requirement than others, which results in the tracking efficiency depending on the particle type.

The use of MC event generators, such as PYTHIA or HIJING, allows to obtain the tracking efficiencies for different particle species as shown in the left panel of Figure 3.7. Here, results from an analysis of the particle dependent efficiency for pp collisions at  $\sqrt{s} = 5.02$  TeV are presented [AAA<sup>+</sup>18]. As shown in the Figure, the dependence of the efficiency on the particle type is strong, especially below 1 GeV/c. In Pb-Pb collisions, similar effects are observed in [Huh17]. Because of these similarities, here the correction procedure is only shown for pp collisions, although an analogous procedure is also implemented for Pb-Pb collisions.

Considering the particle type dependence of the efficiency, the abundance of each particle plays an important role for the particle type inclusive efficiency and must therefore be reflected in the correction. However, MC event generators can't entirely reproduce the production of strange particles [AAAR<sup>+</sup>17]. As a consequence, the efficiency is considerably affected by an underestimation of this production and a correction by means of a reweighting of the efficiency with

the relative abundance of each particle type is implemented. The right plot of Figure 3.7 shows the relative abundances measured in pp collisions recorded by ALICE at  $\sqrt{s}=7$  TeV. This center-of-mass energy is used since no significant energy dependence has been observed experimentally and because of the lack of experimental data at the energy studied in this work [Huh17]. The relative abundances used in this thesis were calculated by the cited analysis using a data-driven procedure and correspond to the same distributions used in the previous ALICE measurement of nuclear modification factors [AAA<sup>+</sup>18].

In summary, the tracking efficiency for inclusive particles should be understood as a weighted superposition of the individual efficiencies for each particle type with the relative particle abundances. Based on this, a  $p_T$ -dependent correction for the efficiencies was determined in [Huh17]. After applying the reweighting on the distributions represented in Figures 3.4 and 3.6 with open symbols, the corrected tracking efficiencies for inclusive charged particles are obtained and shown with full markers. In the bottom panel, the ratio of the reweighted efficiency to the efficiency from pure MC is shown. This reflects the effect of the particle composition correction. The reweighted efficiencies are ultimately utilized to correct the  $p_T$  distributions.

#### 3.4.4 Contamination by secondary particles

The selection procedure described in Section 3.3 aims to reduce the contamination of the measured track sample with secondary particles. Nevertheless, a small amount of these particles persists in it. This remnant originates from weak decays of kaons,  $\Lambda$  baryons and muons as well as from interactions with the detector material. The remaining fraction of secondary particles has to be subtracted from the raw  $p_{\rm T}$  distributions to ensure the purity of the data.

The contamination by secondaries is estimated using the MC productions anchored to the analysed data periods. In Figure 3.8, the secondary contamination from pure MC is shown with open markers for pp collisions as well as for central (0-5%), semi-central (30-40%) and peripheral (70-80%) Pb-Pb collisions. In general, the contamination reaches a value of around 10% in the first  $p_T$  interval. The distributions then fall monotonously with increasing  $p_T$  below 1% in the high  $p_T$  region. These observations are consistent with the assumption that secondaries are inclined to carry small momenta since they correspond essentially to fractions of the momenta of the mother particles or are created in interactions with the detector material. In Pb-Pb collisions, the contamination depends on the centrality. At low  $p_T$ , the contamination in central collisions (0-5%) amounts to almost twice as much as the contamination in the most pe-

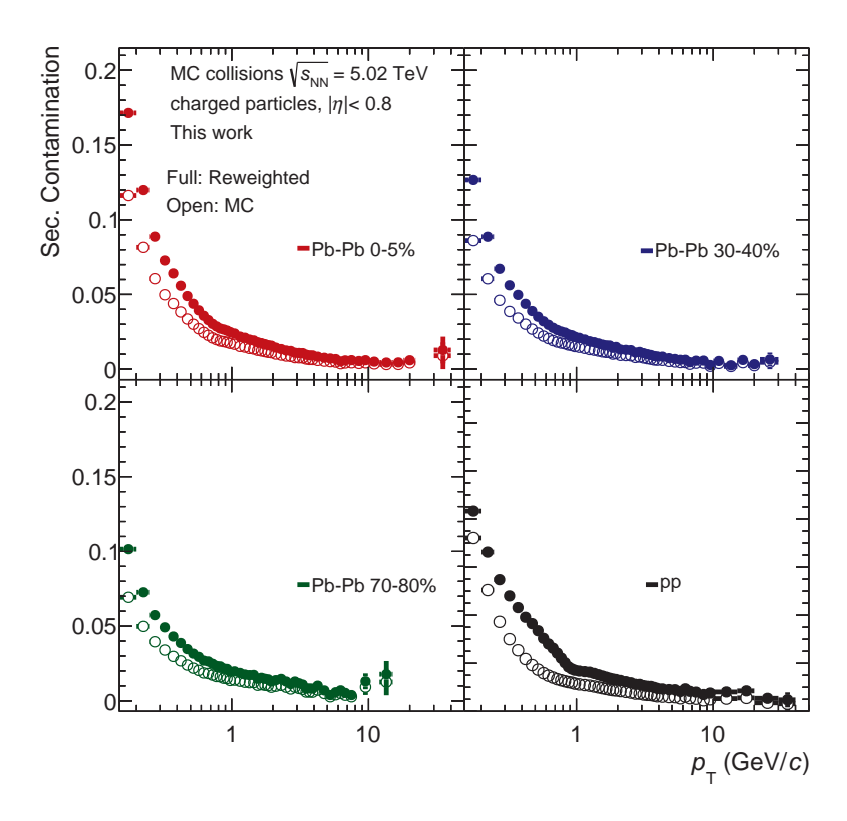


Figure 3.8: Contamination with secondary particles as function of the transverse momentum obtained from MC simulations for pp collisions as well as central, semi-central and peripheral Pb-Pb collisions. Open markers represent the secondary contamination obtained from pure MC, while the full ones correspond to the corrected contamination.

ripheral (70 - 80 %) collisions. This is a result of an enhancement of the yield of strange particles observed in systems with high energy densities. The centrality dependence becomes less pronounced in the high  $p_{\rm T}$  range.

#### Secondary scaling

As stated in the previous section, MC productions underestimate the yield of strange particles. Since the decay products of strange particles are highly prevalent among secondaries, the distributions shown in Figures 3.8 do not reflect entirely the true secondary contamination. To correct for this effect, first, the relative abundance  $\rho_{\text{Data}}$  of secondaries in data is determined in each  $p_{\text{T}}$  interval using the approach explained below. Then, a scaling factor is calculated as:

$$c_{\text{sec. sca.}} = \frac{\rho_{\text{Data}}}{\rho_{\text{MC}}} \tag{3.6}$$

2021080

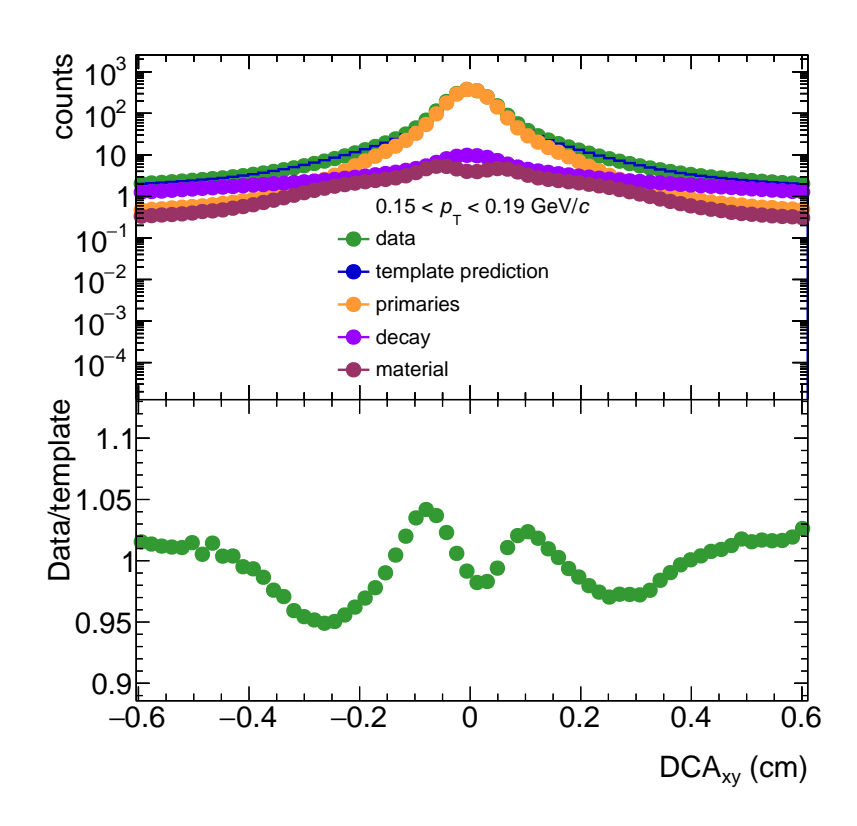


Figure 3.9: DCA<sub>xy</sub> distributions for data and MC simulations for pp collisions at  $\sqrt{s} = 5.02$  TeV for the  $p_{\rm T}$  range  $0.15 \le p_{\rm T} \le 0.19$  GeV/c. The MC predictions correspond to primaries, secondaries from decay and secondaries from interactions in the detector material. In the bottom panel, the ratio of distribution for data to the fit resulting from the MC templates is shown.

where  $\rho_{MC}$  represents the fraction of secondaries in the MC sample. The secondary contamination from pure MC is then reweighted in each  $p_T$  interval with the corresponding scaling factor.

The distance of closest approach (DCA) is used as baseline to discriminate between primaries and secondaries in the data sample. By that, the required fraction  $\rho_{\text{Data}}$  can be determined. Since secondaries originate at a later stage than primaries, the respective DCA<sub>xy</sub> distributions present distinct shapes. The differences should arise particularly in the region of the tails, where the largest DCA<sub>xy</sub> values are located. In this regard, the track selection must be modified in order to obtain a statistically significant result. In particular, the new track selection dispenses with the cuts on the DCA<sub>xy</sub> and on the  $\chi^2_{\text{TPC-ITS}}$ , both of which suppress the yield of secondaries. This modification of the track selection allows to measure an amount of secondaries sufficiently large to extract scaling factors for a few intervals at low  $p_{\text{T}}$  in the range  $0.15 \le p_{\text{T}} < 1.5 \text{ GeV}/c$ .

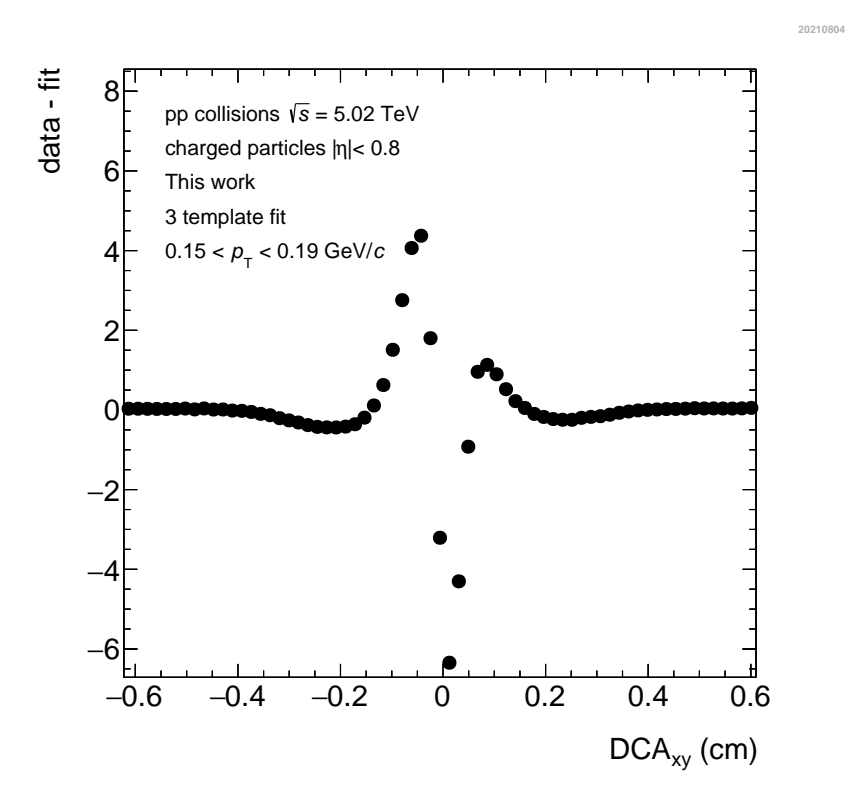


Figure 3.10: Deviation of the template fit from the data points as function of the DCA in pp collisions for the  $p_{\rm T}$  interval  $0.15 \le p_{\rm T} \le 0.19$  GeV/c.

In the upper panel of Figure 3.9, the DCA<sub>xy</sub> distribution for pp collisions recorded by ALICE is illustrated for the  $p_{\rm T}$  interval  $0.15 \le p_{\rm T} \le 0.19$  GeV/c. In the same figure, the corresponding MC predictions of the DCA<sub>xy</sub> in pp collisions for primaries, secondaries from decays and secondaries originating from interactions in the detector material are represented. Primaries present a shape with a prominent peak at 0 cm that far exceeds the small peaks that characterize both distributions of secondaries. Differences are also noticeable towards larger DCA<sub>xy</sub>, where secondaries, as expected, exhibit much broader tails. The data distribution clearly resembles the shape for primary particles since these dominate the particle production.

Next, the DCA<sub>xy</sub> distribution in data is fitted with a linear combination of the MC templates [CERe]. This method takes into consideration statistical uncertainties both from data and MC for a more accurate template fit. The resulting template fit provides as a result the wanted fraction  $\rho_{\text{Data}}$ , which allows for the calculation of the scaling factor  $c_{\text{sec. sca.}}$ . The lower panel of Figure 3.9 shows the ratio of the distribution for data to the result of the template fit.

The intervals of the  $DCA_{xy}$  distributions as well as the  $p_T$  intervals for which the fit is performed are adjusted by minimizing the deviation of the data points from the fit as function of the  $DCA_{xy}$  as shown in Figure 3.10. Here, it can be

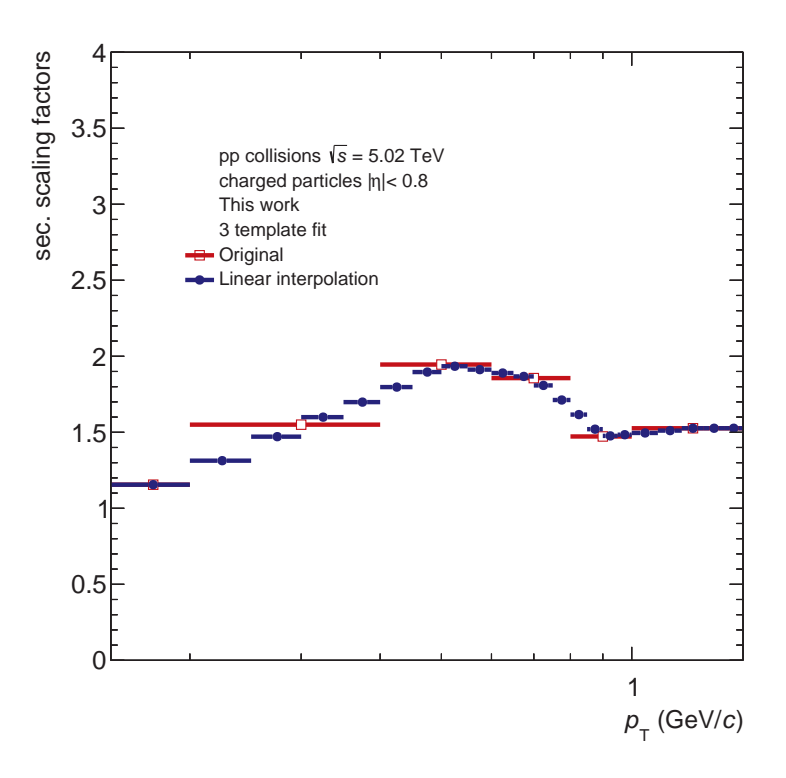


Figure 3.11: Scaling factors used in pp collisions for the correction of the secondary contamination before and after a linear interpolation.

seen that the template fit is in good agreement with the data points in the tails, the region of interest in this approach.

To ensure the goodness of the fit, a Pearson's chi-squared test was performed with a significance level of 0.05. In this approach, the test statistic ratio  $\chi^2$  is computed as follows:

$$\chi^2 = \sum_{i} \frac{(DCA_{data,i} - DCA_{fit,i})^2}{DCA_{fit,i}}$$
(3.7)

Following this, the critical  $\chi^2$  value is calculated by means of the chi-squared probability distribution function determined by the number of degrees of freedom in the fit and the significance level. According to the chi-squared test, the evaluated fit is rejected whenever the test statistic  $\chi^2$  exceeds the critical  $\chi^2$  value. All fits used for the calculation of the scaling factors are statistically significant according to this test.

In Figure 3.11, the resulting scaling factors in pp collisions are shown in the considered  $p_{\rm T}$  intervals with red open markers. In Pb-Pb collisions, the same approach is used. Given that the  $p_{\rm T}$  spectra are represented with a much finer granularity in  $p_{\rm T}$ , the scaling factors are reconstructed through a linear interpolation as shown in this same figure with blue full markers. For  $p_{\rm T} > 1.5~{\rm GeV}/c$ ,

the scaling factor of the last  $p_T$  interval is used since the amount of secondaries barely varies beyond this range. The corrected contaminations by secondaries are shown in Figure 3.8 with full markers.

#### 3.4.5 Transverse momentum resolution

As discussed in Section 2.2.5, the determination of the inverse of the transverse momentum is affected by a measurement uncertainty. Both track parameters are stored during the tracking procedure and can be used to determine the relative momentum resolution by means of Equation 2.4. In Figure 3.12, the distribution of  $\sigma(p_T)/p_T$  is shown as function of  $p_T$  for the analysed pp collisions. The three visible structures at low  $p_T$  can be explained by the interaction of charged particles with the detector material of the ITS. When a particle crosses the detector, it undergoes multiple scattering and its trajectory is consequently deflected by small angles affecting thereby the track parameters determination. Such an effect is dependent on the particle mass and the observed distinct trends of the resolution correspond, in decreasing order of uncertainty, to protons, kaons and pions. For a clearer representation, the mean value  $\langle \sigma(p_T)/p_T \rangle$  of this distribution is calculated in each  $p_T$  interval. As a result, the mean relative  $p_T$  resolution as function of  $p_T$  is obtained as shown in Figure 3.13. At low  $p_T$ , the relative p<sub>T</sub>-resolutions are influenced mainly by the multiple scattering of the charged particles in the detector material. In this region, the results in pp and Pb-Pb as well as among the different centrality classes resemble each other as shown in (cit mknichel). At  $p_T = 0.15 \text{ GeV}/c$ , the resolution is on average around 3.7 %.

The effect of the multiple scattering dissipates gradually until the distribution hits the minimum around 1.5 GeV/c with a  $p_{\rm T}$  resolution of around 0.7 % in pp and 0.8 % in Pb-Pb. At high  $p_{\rm T}$ , charged particles experience a less pronounced curvature according to Equation 2.1, which causes a deterioration of the spatial resolution. As a consequence, the uncertainty grows linearly reaching values of 4.4 % in pp and 5.4 % in Pb-Pb.

Since the measurement of  $p_{\rm T}$  is smeared due to the resolution, the  $p_{\rm T}$  spectra must be corrected accordingly. While the smearing has a minor effect on the  $p_{\rm T}$  spectra at low  $p_{\rm T}$  given the smooth slope of the distributions, it becomes more pronounced in the high  $p_{\rm T}$  region, where the  $p_{\rm T}$  spectra describe a steeply falling shape. The corresponding correction is thus applied in the range  $7 \le p_{\rm T} \le 100$  GeV/c by means of a  $p_{\rm T}$ -dependent factor  $c_{\rm reso}$  calculated as follows:

$$c_{\text{reso}}(p_{\text{T}}) = \frac{(dN/dp_{\text{T}})_{\text{smeared}}}{(dN/dp_{\text{T}})_{\text{true}}}$$
(3.8)

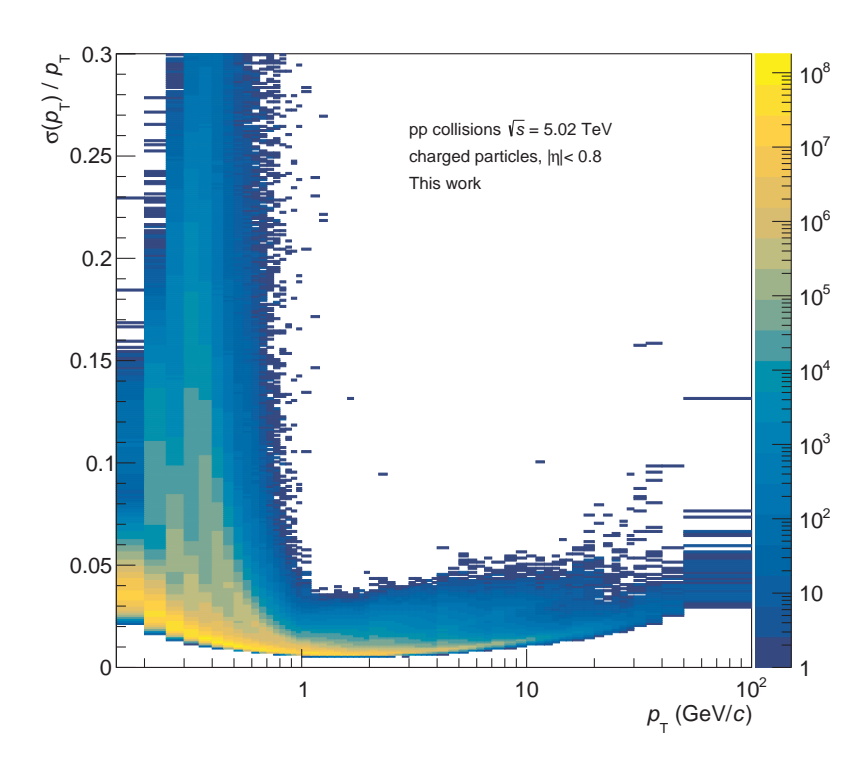


Figure 3.12: Transverse momentum resolution as function of the transverse momentum for pp collisions at  $\sqrt{s} = 5.02$  TeV recorded in ALICE in 2017.

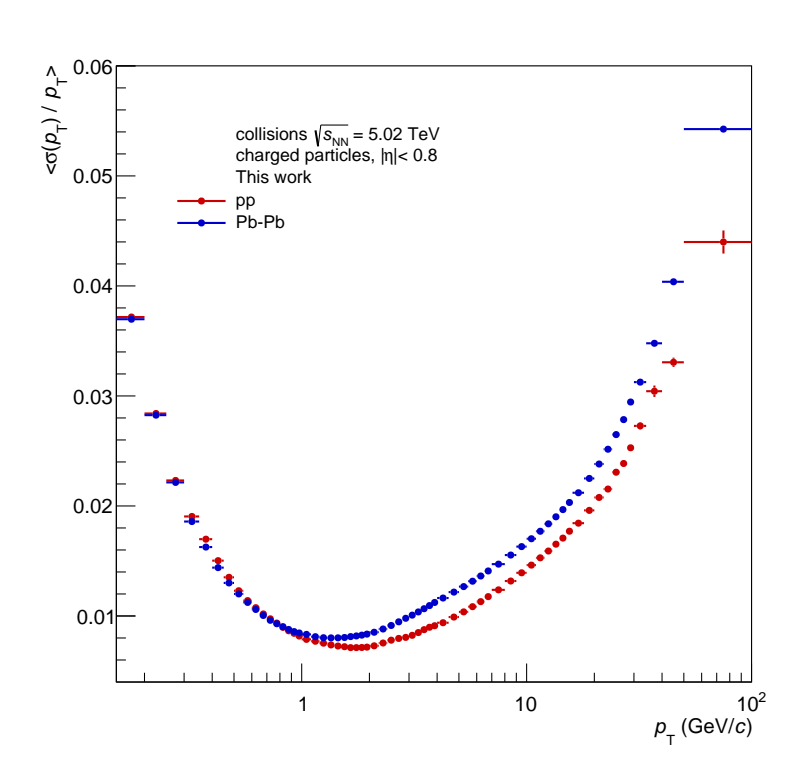


Figure 3.13: The mean relative transverse momentum resolutions are obtained as function of the transverse momentum for pp and MB Pb-Pb collisions.

where the numerator corresponds to the measured  $p_T$  distribution, while the denominator is a  $p_T$  distribution free of smearing. As starting point, the  $p_T$  distributions from the previous ALICE  $R_{PbPb}$  measurement [AAA+18] are used, given that they already corrected for the effect of the  $p_T$  resolution and thus offer an approximation of the true  $p_T$  distributions. For the calculation of  $c_{reso}(p_T)$ , these  $p_T$  distributions are smeared using a simulation to emulate the effect of the  $p_T$  resolution on the  $p_T$  distributions. The details of this procedure are outlined in the following.

#### Calculation of the correction factor

The smearing is carried out through a simulation that uses as input a sample of filtered high  $p_{\rm T}$  tracks that underwent the same track requirements as summarized in Table 3.2. The parameter  $\sigma(1/p_{\rm T})$  of these tracks is obtained as function of  $1/p_{\rm T}$  as shown in the top-left panel of Figure 3.14 for the case of pp collisions. This two-dimensional representation is converted to a distribution of the mean uncertainty  $\langle \sigma(1/p_{\rm T}) \rangle$  as function of  $1/p_{\rm T}$ . Next, this distribution is parametrized with a 2nd order polynomial  $n(1/p_{\rm T})$  which is subtracted from the original uncertainty  $\sigma(1/p_{\rm T})$  to exclude the  $p_{\rm T}$  dependence and, by that, reduce statistical fluctuations as seen in the top-right panel of Figure 3.14. The scaled  $\sigma(1/p_{\rm T})$  distribution (bottom left panel of Figure 3.14) is subsequently projected into the y-axis obtaining thereby a distribution that reveals the probability function of  $\sigma(1/p_{\rm T})$  as shown in the bottom-right panel of Figure 3.14.

After determining the shape of  $\sigma(1/p_{\rm T})$  without the  $p_{\rm T}$  dependence, the smearing is performed. In this process, simulated tracks are distributed according to a power-law fit of the true  $p_{\rm T}$  distributions in the range  $7 \le p_{\rm T} \le 100$  GeV/c. These are then transformed in  $1/p_{\rm T}$  distributions. Each  $1/p_{\rm T}$  value is smeared according to a Gaussian with a standard deviation generated randomly based on the probability function of  $\sigma(1/p_{\rm T})$ . This standard deviation is then adjusted adding a factor extracted from an evaluation of the polynomial  $n(1/p_{\rm T})$  as recorrection for the above mentioned suppression of statistical fluctuations (bottom-left panel of Figure 3.14 ). Finally, the smeared  $1/p_{\rm T}$  distribution is reconverted in a  $p_{\rm T}$  spectrum, which corresponds to the numerator of Equation 3.8.

In Figure 3.15, the resulting correction factors as defined in Equation 3.8 for pp and for central, semi-central and peripheral Pb-Pb collisions are illustrated. The correction factor falls monotonically and the effect finds its maximum at the largest  $p_{\rm T}$  interval with a value of around 1.2 % (1 %) for pp (Pb-Pb) collisions. The Pb-Pb results show a similar trend as in the pp data collection. Nevertheless, a centrality dependence of the correction factors is observed which originates from the different steepness of the true  $p_{\rm T}$  spectra.

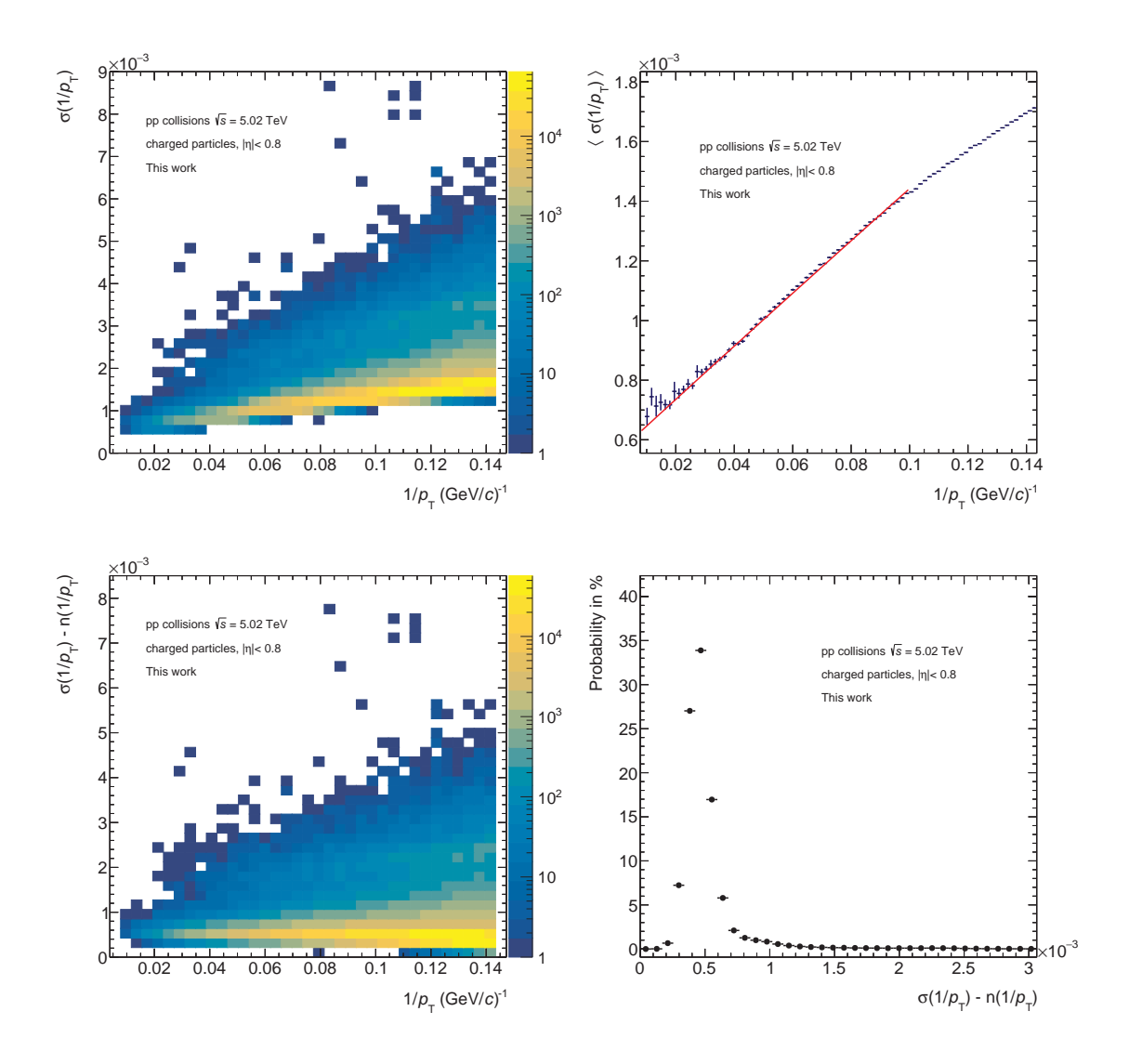


Figure 3.14: **Top.** Left: Two-dimensional distribution of the uncertainty on the inverse of the transverse momentum  $\sigma(1/p_{\rm T})$  as function of  $1/p_{\rm T}$ . Right: 2nd order polynomial parametrization  $n(1/p_{\rm T})$  of the mean uncertainty  $\langle \sigma(1/p_{\rm T}) \rangle$  as function of  $1/p_{\rm T}$ . **Bottom.** Left: Two-dimensional distribution of the scaled uncertainty  $\sigma(1/p_{\rm T})$  as function of  $1/p_{\rm T}$ . Right: Probability function of  $\sigma(1/p_{\rm T})$  obtained after projecting the scaled uncertainty into the *y*-axis.

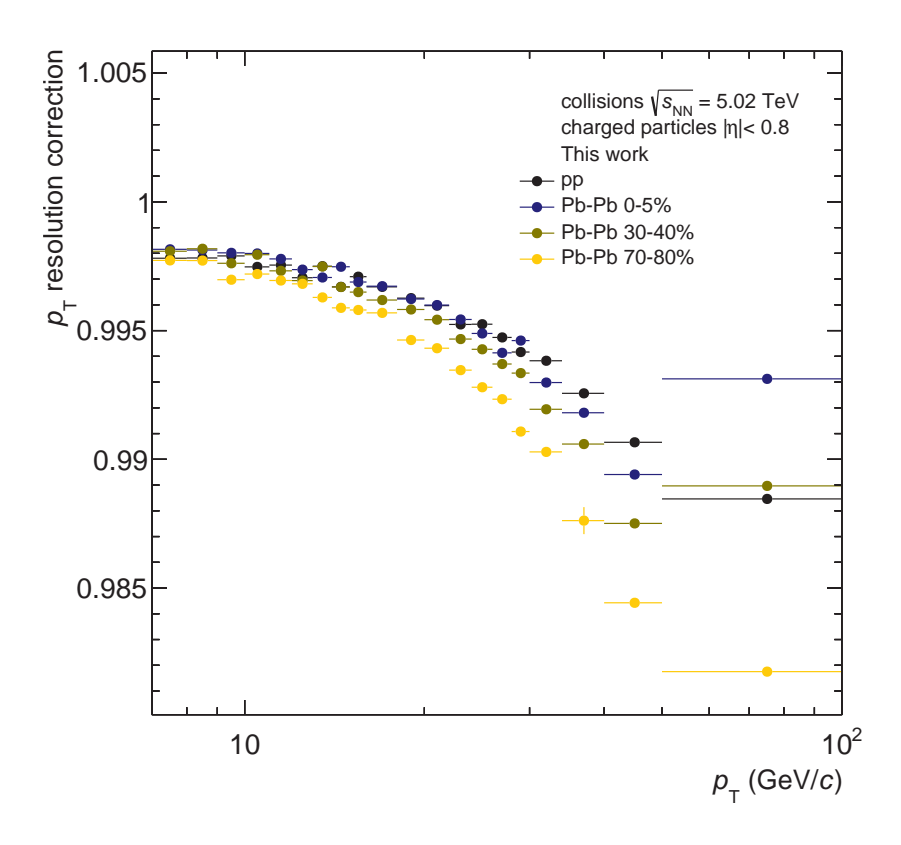


Figure 3.15:  $p_{\rm T}$  resolution correction factor as function of  $p_{\rm T}$  in pp and in three centrality classes of Pb-Pb collisions at  $\sqrt{s_{\rm NN}}=5.02$  TeV recorded in ALICE.

## 3.5 Implementation of the corrections

As already mentioned, the track-level corrections affect the shape of the primary track distribution  $N_{\text{raw}}(p_{\text{T}})$ . The corrected primary track distribution  $N_{\text{corr}}(p_{\text{T}})$  can be defined as follows:

$$N_{\text{corr}}(p_{\text{T}}) = N_{\text{raw}}(p_{\text{T}}) \times \frac{1}{\epsilon(p_{\text{T}}) \cdot c_{\text{par comp}}(p_{\text{T}})} \times (1 - c_{\text{cont}}(p_{\text{T}}) \cdot c_{\text{sec. sca.}}(p_{\text{T}})) \times \frac{1}{c_{\text{reso}}(p_{\text{T}})} \times \frac{1}{\chi_{\text{sig loss}}(p_{\text{T}})}$$
(3.9)

where  $\epsilon(p_{\rm T})$  is the tracking efficiency,  $c_{\rm par\ comp}(p_{\rm T})$  the particle composition correction,  $c_{\rm cont}(p_{\rm T})$  the secondary contamination correction,  $c_{\rm sec\ sca}(p_{\rm T})$  the secondary scaling,  $c_{\rm reso}(p_{\rm T})$  the  $p_{\rm T}$  resolution correction and  $\chi_{\rm sig\ loss}(p_{\rm T})$  the signal loss, which is only applied in pp collisions. The implementation of these equations leads to the fully corrected  $p_{\rm T}$  distributions in pp and Pb-Pb collisions. The results in pp collisions are expressed in form of a differential cross section:

$$\frac{d^{2}\sigma_{\text{ch}}^{\text{pp}}}{d\eta dp_{\text{T}}} = \sigma_{\text{vis}} \cdot \frac{1}{N_{\text{INEL}}} \cdot \frac{d^{2}N_{\text{corr}}^{\text{pp}}}{d\eta dp_{\text{T}}}$$

$$= \sigma_{\text{vis}} \cdot \frac{\epsilon_{\text{Trig}} \cdot \epsilon_{\text{Vz}}}{N_{\text{ev}}^{\text{rec}}} \cdot \frac{d^{2}N_{\text{corr}}^{\text{pp}}}{d\eta dp_{\text{T}}}$$
(3.10)

where  $N_{\rm INEL}$  corresponds to the total number of inelastic events and  $\sigma_{\rm vis}$  the visible inelastic cross section discussed in Section 3.4.1. In the case of Pb-Pb collisions, the results are presented as invariant yields which are calculated as follows

$$\frac{d^{2}N_{\text{ch}}^{\text{Pb-Pb}}}{d\eta dp_{\text{T}}} = \frac{1}{N_{\text{INEL}}} \cdot \frac{d^{2}N_{\text{corr}}^{\text{Pb-Pb}}}{d\eta dp_{\text{T}}}$$

$$= \frac{1}{N_{\text{ev}}^{\text{rec}}} \cdot \frac{d^{2}N_{\text{corr}}^{\text{Pb-Pb}}}{d\eta dp_{\text{T}}}$$
(3.11)

Note that both trigger and vertex reconstruction efficiency are unity in Pb-Pb collisions as explained in Section 3.4.1.

The differentials  $d\eta$  and  $dp_T$  in Equations 3.10 and 3.11 are approximated with the full  $\eta$ -range  $\Delta \eta = 1.6$  and the width of the  $p_T$  interval  $\Delta p_T$ , respectively.

## 3.6 Systematic uncertainties

MC simulations aim to reproduce accurately the detector performance so that their information can be used to correct the data. The resulting corrections are validated by accounting for systematic uncertainties. For the measurement of nuclear modification factors of charged particles several sources of systematic uncertainties have been identified in previous measurements on the topic by the ALICE Collaboration. In this thesis, a focus has been laid upon the systematic evaluation of uncertainties from the assumptions made for the track selection criteria. Additional sources of systematic uncertainties as investigated in [AAA<sup>+</sup>18] have not been evaluated for the  $p_T$  distributions in this work, yet, and need additional extensive studies in the future. These systematics uncertainties are related to the tracking efficiency, the particle composition correction, the secondary scaling, the trigger and vertex reconstruction efficiency, the material budged in MC simulations and the anchor point. As an estimate these additional sources of uncertainties and their range of contribution to the systematic uncertainties to the  $p_{\rm T}$  distributions corresponding to the maximal variation obtained in [AAA<sup>+</sup>18] are presented later in this chapter.

#### 3.6.1 Track selection

As explained in Section 3.3, the track selection criteria have been developed and validated in the course of the last years. Nevertheless, the choice of the selection criteria, yet justified via cross-checks, is subjected to a systematic uncertainty. The total value of  $\sigma_{\text{tot}}^{\text{sys}}$  is calculated via the root sum squared method over the individual contributions to the systematic uncertainties, which are assumed to contribute independently of the rest. For this reason, :

$$\sigma_{\rm sel,tot}^{\rm sys} = \sqrt{\sum_{\rm i} \left(\sigma_{\rm sel,i}^{\rm sys}\right)^2}$$
 (3.12)

To determine the individual contributions, each nominal track requirement listed in Table 3.2 is varied twice within a range in which it is believed to be physically meaningful. The variations, listed in Table 3.4, correspond to the maximum and the minimum of this range. Next, the fully corrected  $p_T$  distributions are recalculated with each variation. The ratio of these  $p_T$  spectra to the nominal one is determined, obtaining as a result two ratios for each track cut, with the exception of the required hit in the SPD. The two ratios are evaluated in each  $p_T$  interval and the largest deviation from the nominal  $p_T$  spectrum between both of them is assumed as systematic uncertainty in the corresponding

Track parameter	Condition	Variations				
Selection of primaries						
$DCA_z$	≤ 2 cm	1 cm	5 cm			
$DCA_{xy}$	$\leq 7\sigma$	$4\sigma$	$10\sigma$			
ITS selection						
at least one hit in the SPD	required	not re	quired			
$\chi^2$ per ITS cluster	< 36	≤ <b>2</b> 5	$\leq 49$			
TPC selection						
$\chi^2$ per TPC cluster (pp collisions)	< 4.0	≤ 3.0	≤ 5.0			
$\chi^2$ per TPC cluster (Pb-Pb collisions)	< 2.5	≤ 1.7	≤ 3.4			
fraction of shared TPC clusters	< 0.4	$\leq 0.2$	$\leq 1.0$			
ratio of crossed rows over findable clusters	> 0.8	$\geq 0.7$	$\geq 0.9$			
geometric length (dead TPC area)	3 cm	2 cm	4 cm			
geometric length (track length)	130 cm	120 cm	140 cm			
TPC-ITS selection						
$\chi^2$ TPC constrained track vs. global track	≤ 36	≤ 25	≤ <b>4</b> 9			

Table 3.4: Variations for the standard track selection criteria used for the calculation of the systematic uncertainties.

 $p_{\rm T}$  interval. The resulting systematic uncertainties corresponding to each track cut can then be presented as function of the transverse momentum. In Figure 3.16, the individual contributions and the combined systematic uncertainty are given for pp as well as for central, semi-central and peripheral Pb-Pb collisions. In the previous ALICE measurement of nuclear modification factors, the corresponding systematic uncertainties were calculated by propagating the systematic uncertainties on the  $p_{\rm T}$  distributions in pp and Pb-Pb collisions. With the aim of obtaining a more accurate estimation of the systematic uncertainties on  $R_{\rm Pb-Pb}$ , the same approach explained above is used. In Figure 3.17, the resulting contributions are shown for pp as well as for central, semi-central and peripheral Pb-Pb collisions.

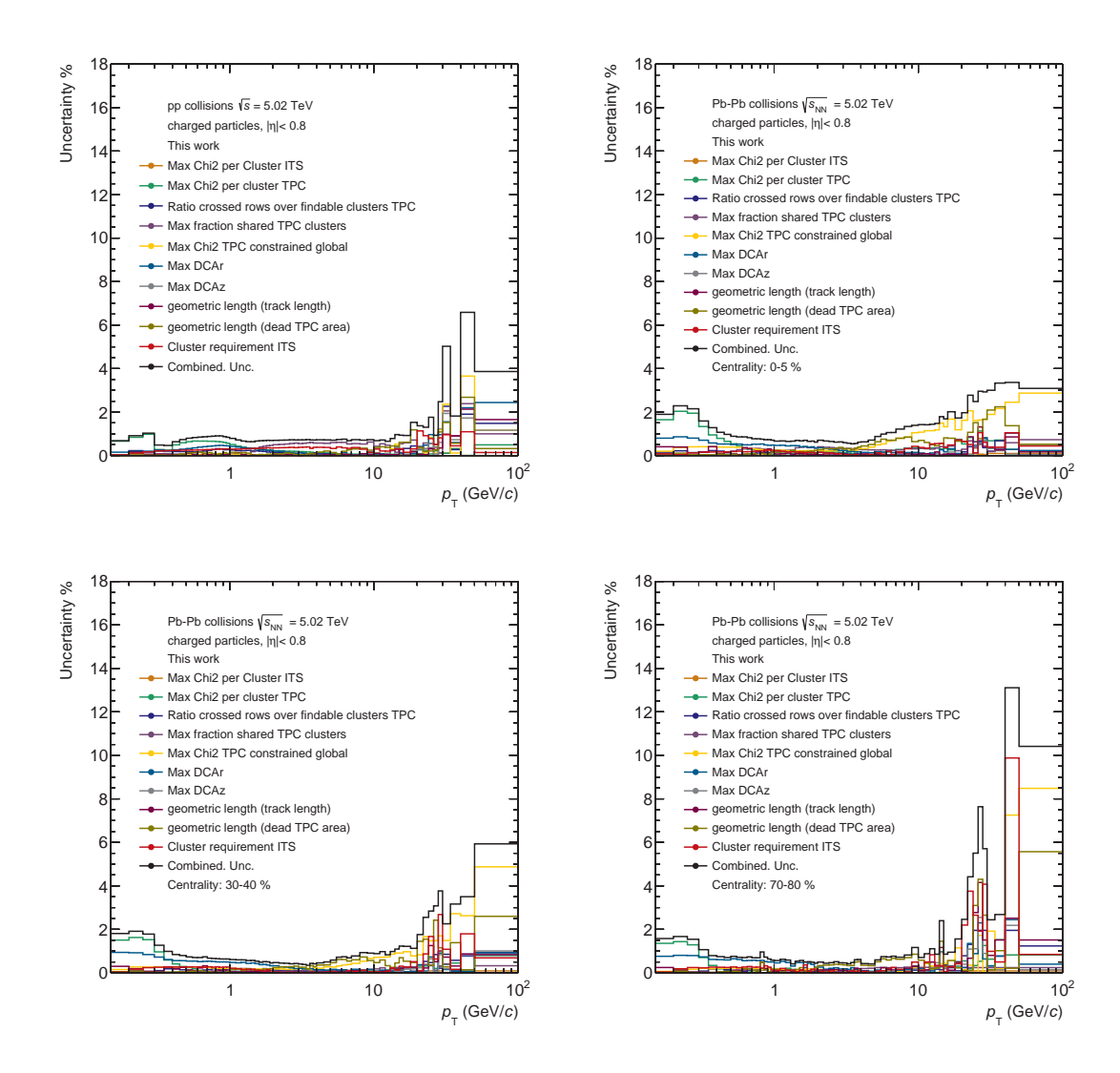


Figure 3.16: Relative systematic uncertainties of the  $p_T$  spectra from the track selection for pp as well as central, semi-central and peripheral Pb-Pb collisions.

#### 3.6.2 Other sources of uncertainties

In previous measurements of inclusive charged particles [AAA<sup>+</sup>18], other sources of systematic uncertainties on the  $p_{\rm T}$  distributions besides the track selection have been identified. In this section, an overview about the corresponding sources as well as an approximation of their contributions to the total systematic uncertainties acquired from the cited publication will be given. Nevertheless, as already mentioned at the beginning of the chapter, these contributions aren't applied to the final results of this thesis. In Table 3.5, the range of the maximal variation are shown within a  $p_{\rm T}$  range of  $0.15 \le p_{\rm T} \le 50~{\rm GeV}/c$  for pp and Pb-Pb collisions.

• The tracking efficiency is approximated using the MC information. Nevertheless, the simulations are not able to reproduce fully the detector per-

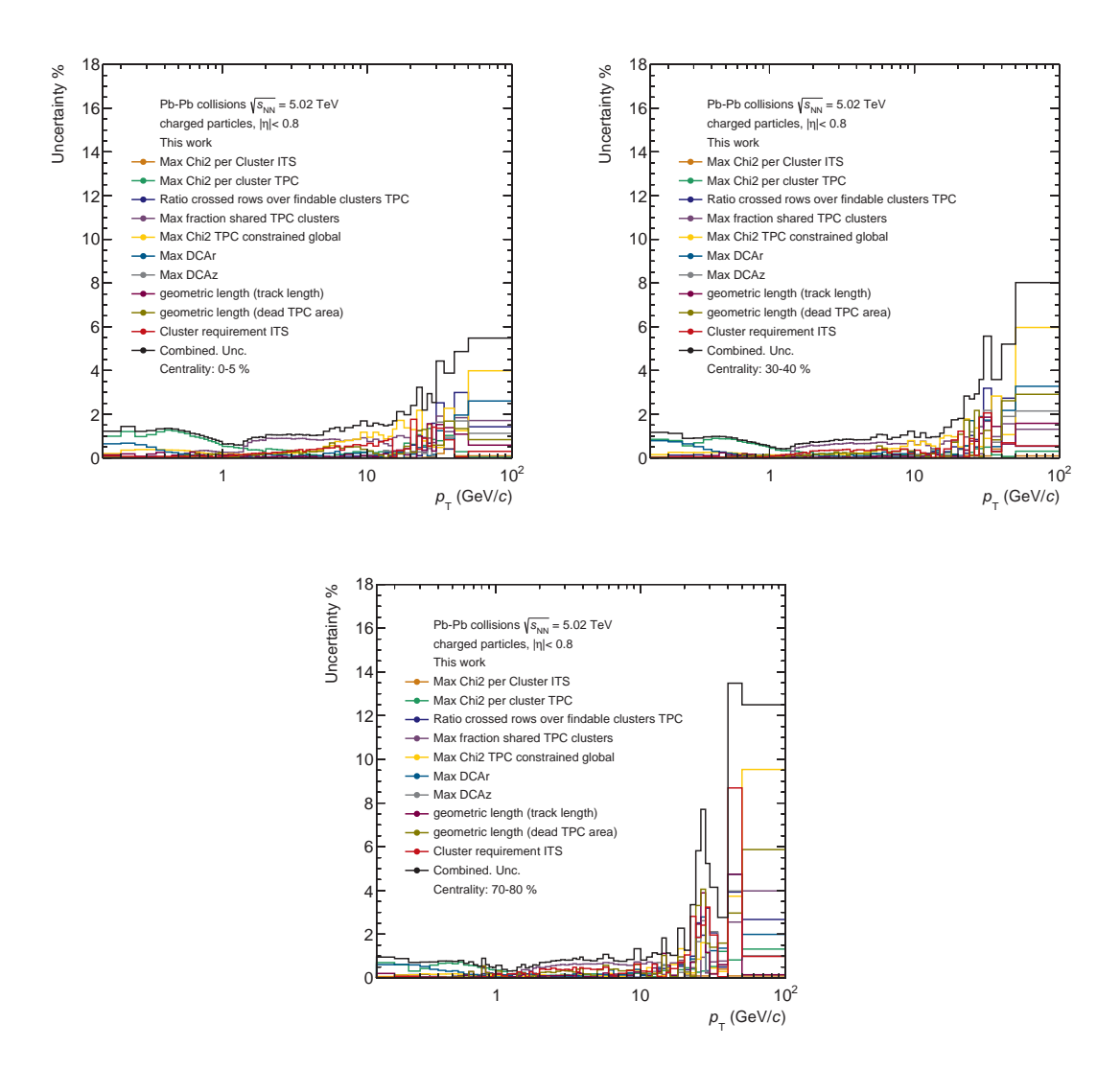


Figure 3.17: Relative systematic uncertainties of  $R_{PbPb}$  from the track selection for central, semi-central and peripheral Pb-Pb collisions.

formance. The related systematic uncertainty is calculated by means of a quantity that compares ITS-TPC tracks with tracks reconstructed only with the TPC: the matching efficiency. The maximum deviation from unity of the ratio of the matching efficiency in MC to the one in data is used as uncertainty.

• In the analysis presented in [Huh17], three distinct contributions to the systematic uncertainty of the particle composition correction are considered. The contributions are related to assumptions during the development of the analysis. For their calculation, variations in specific parameters of the procedure are performed and the maximal deviation between the nominal correction and the one resulting from each variation is assigned as systematic uncertainty. The total systematic uncertainty is determined by summing in quadrature the individual contributions.

Source of uncertainty	pp	Pb-Pb	
Matching efficiency	0.0-1.1%	0.2-1.2%	
Particle composition	0.2-2.4%	0.2-2.0%	
Secondary scaling	0.0-2.8%	0.0-4.5%	
Vertex and trigger efficiency	0.0-1.2%	-	
Material budget	0.1-0.9%	0.1-0.9%	
Anchor point	-	0.06-3.5%	

Table 3.5: Contributions to the total systematic uncertainty on  $p_T$  distributions in pp and Pb-Pb collisions determined in the previous ALICE measurements [AAA<sup>+</sup>18] shown within a  $p_T$  range of  $0.15 \le p_T \le 50 \text{ GeV}/c$ .

- The contribution to the systematic uncertainties of the data-driven scaling
  of the secondary contamination is determined by comparing the correction factors that result from a two and a three template fit. The deviation
  between both results is assigned as uncertainty.
- In the published results, the vertex and trigger efficiency is combined and the half of this value was assigned as systematic uncertainty.
- The MC simulation of the detector response by the GEANT3 framework bears an uncertainty, which is determined by varying the material budget by  $\pm 4.5\%$ .
- For the centrality determination in Pb-Pb collisions, an anchor point is defined as the reference limit of the centrality below which the measurement is biased (Section 2.2.6). Its determination is subject to an uncertainty of 0.5%. After adjusting the centrality boundaries with this uncertainty, p<sub>T</sub> spectra are recalculated and the maximum deviation from the nominal one is assigned as the corresponding contribution.

### 3.7 Results

## 3.7.1 Differential cross section in pp collisions

After implementing the corrections as described in Section 3.5, the differential cross section (Equation 3.10) for inclusive charged particles in inelastic pp collisions at  $\sqrt{s} = 5.02$  TeV measured by ALICE is presented in Figure 3.18. The statistical uncertainties are shown in error bars, while the boxes represent the

systematic uncertainties determined as described in Section 3.6.1. In the figure, the previous ALICE measurement [AAA<sup>+</sup>18] is also shown. It can be observed that the presented work reaches a transverse momentum of  $p_T = 100 \text{ GeV}/c$  which extends the  $p_T$  reach of the previous measurement of  $p_T = 50 \text{ GeV}/c$ . This is explained by the higher statistics of the data sets in comparison to the ones used in the previous ALICE measurement of nuclear modification factors. Another feature of this result is the improved granularity of the  $p_T$  intervals which are finer in the mid and high  $p_T$  region than in the previous measurements. These two aspects facilitate a better precision of the nuclear modification factors as it will be seen in the following sections.

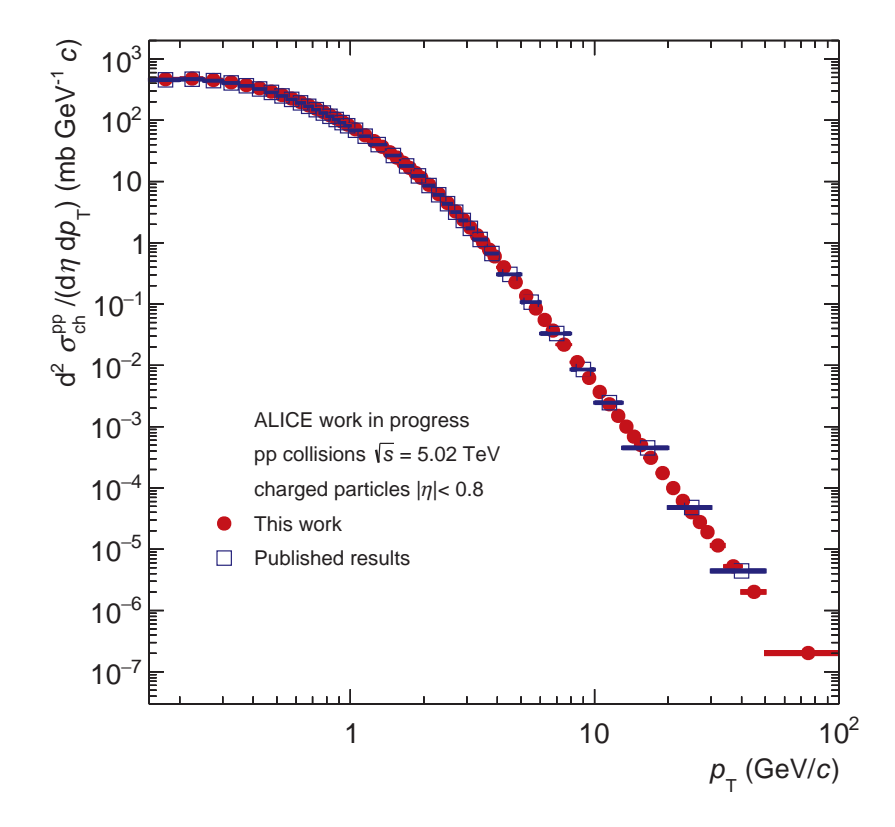


Figure 3.18: Differential cross section for inclusive charged-particle production in pp collisions at  $\sqrt{s} = 5.02$  TeV measured by ALICE.

### 3.7.2 Invariant yield in Pb-Pb collisions

The invariant yields (Equation 3.11) for inclusive charged particles in nine centrality classes in inelastic Pb-Pb collisions measured by ALICE at  $\sqrt{s_{\mathrm{NN}}} = 5.02$  TeV are given in Figure 3.19. Statistical and systematic uncertainties are represented with error bars and boxes, respectively. In the same figure, the results of the previous ALICE measurement are also shown. The shape of

the  $p_{\rm T}$  distributions show a strong centrality dependence. In central collisions, the invariant yields present a more pronounced slope for  $p_{\rm T} > 3~{\rm GeV/}c$  than the one in peripheral collisions. With decreasing centrality the shape becomes more similar to the one in pp. Once the full corrected  $p_{\rm T}$  distributions in pp and in Pb-Pb collisions are determined, the nuclear modification factors are calculated as discussed in the next section.

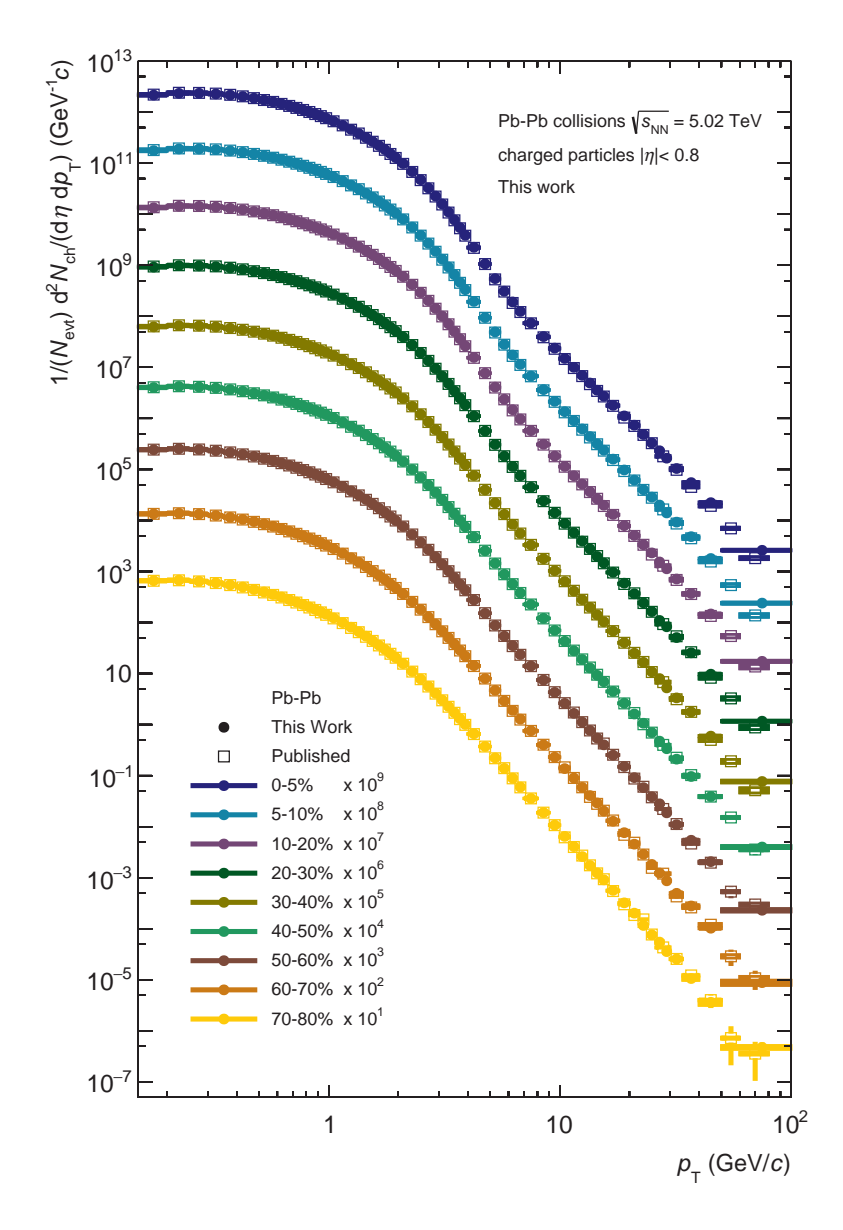


Figure 3.19: Differential cross section for inclusive charged-particle production in pp collisions at  $\sqrt{s} = 5.02$  TeV measured by ALICE.

Centrality	$\langle { m T}_{PbPb}  angle$ (mb $^{-1}$ )	sys. Unc. $(mb^{-1})$		
0-5 %	26.08	0.176		
5-10 %	20.44	0.166		
10-20 %	14.4	0.126		
20-30 %	8.767	0.101		
30-40 %	5.086	0.0814		
40-50 %	2.747	0.0486		
50-60 %	1.352	0.0309		
60-70 %	0.5992	0.0158		
70-80 %	0.2385	0.00552		

Table 3.6: Nuclear overlap function with the corresponding systematic uncertainties for Pb-Pb collisions at  $\sqrt{s}_{\rm NN} = 5.02$  TeV in the studied centrality classes obtained with a Glauber Monte Carlo simulation [ALI18b].

#### 3.7.3 Nuclear modification factors

The energy density produced in ultra-relativistic heavy-ion collisions allows for the creation of a QGP, a deconfined state of strongly interacting matter. In this medium, high  $p_T$  partons experience an energy loss which leads to a suppression of the particle production as discussed in Section 1.5. The study of this suppression can therefore provide insight on the properties of the QGP. In the presented work, the suppression is analyzed by comparing the charged-particle production in heavy-ion collisions with a reference measurement in pp collisions, where no QGP is expected to be created. The nuclear modification factor  $R_{PbPb}$  offers the possibility to quantify the suppression via:

$$R_{\text{PbPb}} = \frac{1}{\langle T_{\text{AA}} \rangle} \frac{d^2 N_{\text{ch}}^{\text{Pb-Pb}} / d\eta dp_{\text{T}}}{d^2 \sigma_{\text{ch}}^{\text{pp}} / d\eta dp_{\text{T}}}$$
(3.13)

where the numerator represents the invariant yield in Pb-Pb collisions and the denominator the differential cross section in pp collisions. Note that the differential cross section is scaled with the nuclear overlap function  $\langle T_{\text{PbPb}} \rangle$ . This quantity is calculated through a Glauber MC simulation [ALI18b] and the values used in this work can be found in Table 3.6.

In Figure 3.20, the nuclear modification factors for inclusive charged particles in inelastic Pb-Pb collisions measured by ALICE at  $\sqrt{s}_{\rm NN}=5.02$  TeV are presented in nine centrality classes. The statistical uncertainties are denoted as error bars

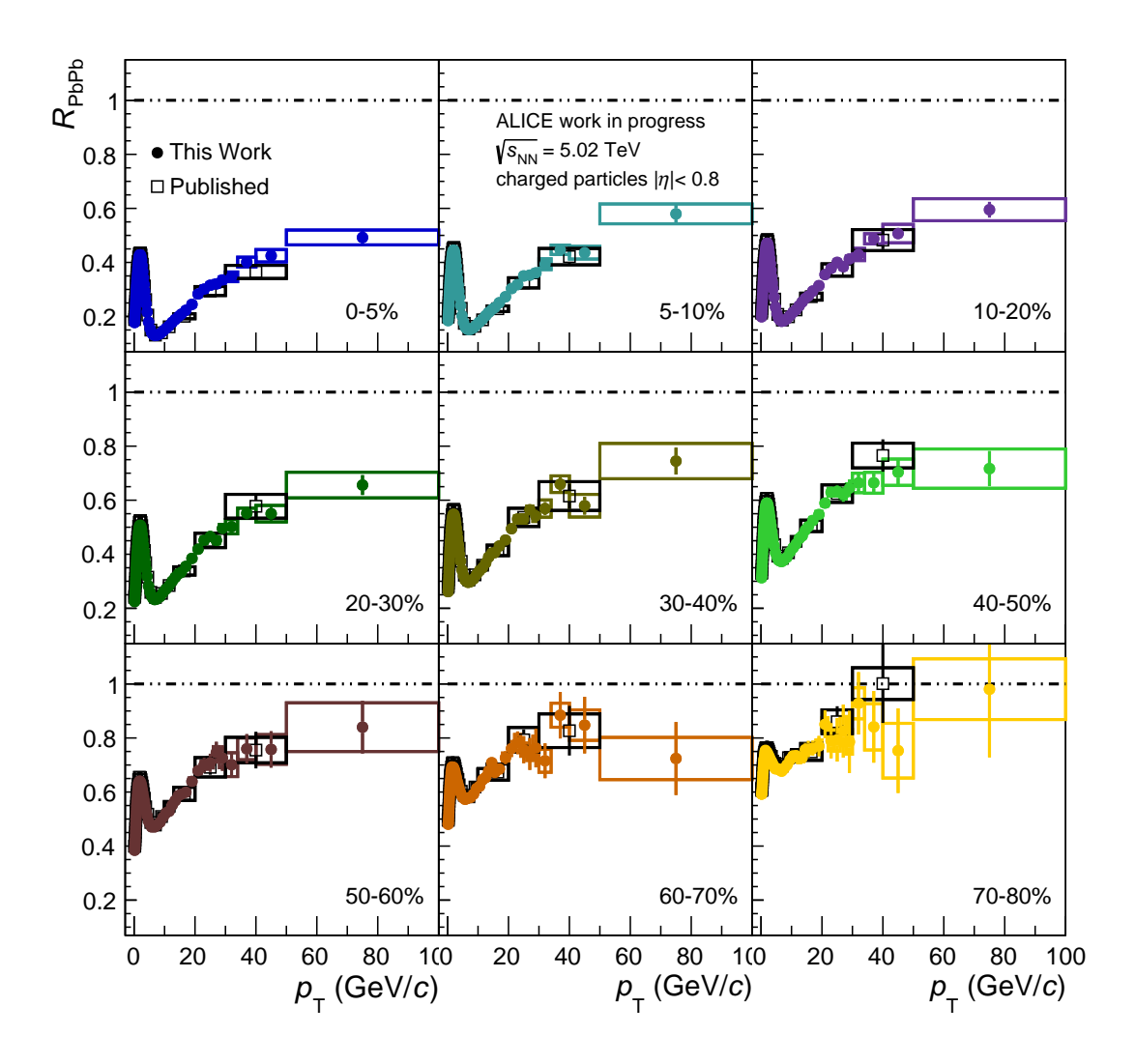


Figure 3.20: Nuclear modification factors for nine centrality classes in Pb-Pb collisions at  $\sqrt{s} = 5.02$  TeV measured by ALICE.

and the systematic uncertainties as boxes. As expected, the nuclear modification factors are characterized by a strong dependency on the centrality. In the same figure, the previous measurements of nuclear modification factors in ALICE are also shown with open markers. The results of this work are in good agreement with the ones of the previous measurement. There is an improvement of the  $p_{\rm T}$  reach as well as of the granularity of the intervals for  $p_{\rm T} > 3.2~{\rm GeV}/c$ . This is a result of the increased statistics in pp collisions which allows for a better precision in the corresponding  $p_{\rm T}$  distribution as described before.

A significant suppression of the charged-particle production is observed in most  $p_{\rm T}$  intervals of the nine centrality classes. In the low  $p_{\rm T}$  region, the suppression decreases slightly until the  $R_{\rm PbPb}$  reach values of around 0.45 in the most central collisions and around 0.8 in peripheral collisions. Following this peak, the max-

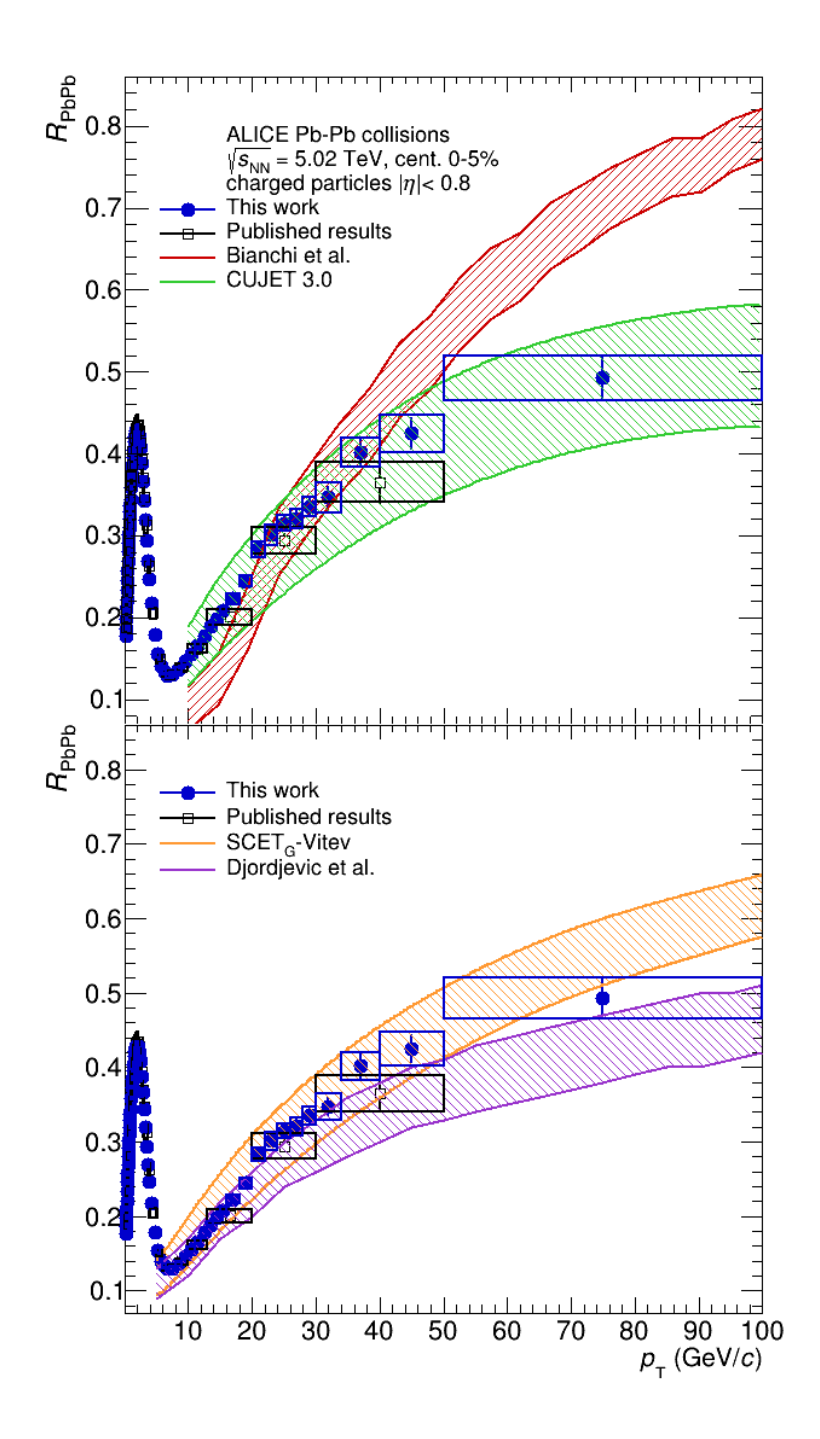


Figure 3.21: Nuclear modification factors for the most central collisions in Pb-Pb collisions at  $\sqrt{s}=5.02$  TeV compared to four theoretical prediction as well as to the previous ALICE publication.

imal suppression occurs at around  $p_T = 6.5 \text{ GeV}/c$  for the first four centrality classes, before the nuclear modification factors rise gradually and reach values between around 0.5 and 0.6. Towards peripheral collisions, the fall after the

peak is less pronounced, the factors grow more steeply and the values of  $R_{PbPb}$ approach unity at high transverse momenta. For a better understanding of the suppression in heavy-ion collisions, several theoretical models make predictions about the influence of the strong interacting medium produced at LHC energies on the charged-particle production. For the validation of the measured nuclear modification factors, is worth comparing them with the theoretical models presented in Section 1.6. In Figure 3.21, the measured nuclear modification factor for a centrality of 0-5 % is compared to the four theoretical models as well as to the previous ALICE measurement. The upper and lower boundaries of the models represent the uncertainty which is calculated through variation of different parameters of the corresponding approaches. The measured nuclear modification factors are overall consistent with CUJET 3.0 and the models of Vitev and Djordjevic. It is worth pointing out, the similar agreement of the Vitev and Djordjevic calculations with the results although only the later includes predictions of the collisional energy loss. On the other hand, the Bianchi's model overestimates the suppression in the  $p_T$  range  $10 < p_T < 18 \text{ GeV}/c$ , a trend already observed in the previous measurements. Nevertheless, the improvements in the nuclear modification factors allow to make a better distinction at very high  $p_T$ . By that, it can be now stated that this model clearly deviates from the measured results since for  $p_T > 50 \text{ GeV}/c$  it also underestimates the data. Therefore, as proposed at the beginning of this work, the increase of the data sample statistics can lead to a better understanding of  $R_{AA}$  in comparison to the theoretical model predictions.

## 4 Summary

In this thesis, the transverse-momentum distributions for non-identified primary charged particles is measured in the kinematic range  $|\eta| < 0.8$  and  $0.15 < p_{\rm T} < 100~{\rm GeV}/c$  in pp and in nine Pb-Pb centrality classes at  $\sqrt{s_{\rm NN}} = 5.02~{\rm TeV}$ . Moreover, nuclear modification factors  $R_{\rm PbPb}$  are determined by calculating the ratio of the  $p_{\rm T}$  distributions obtained in Pb-Pb collisions to the reference measurement in pp collisions scaled with the mean nuclear overlap function  $\langle T_{\rm AA}(b) \rangle$ .

The analysis is making use of pp and Pb-Pb collisions collected by ALICE in the years 2017 and 2018, respectively. The pp data taking consists of two data sets, FAST and CENT, distinguished by their respective readout configurations: while FAST contains events measured excluding the information of the SDD layers, the CENTS events were reconstructed including it. The combination of these subset leads to a significant increase of the statistics which allows for an enlarged  $p_T$  reach of the charged-particle  $p_T$  spectrum in pp collisions. This improvement is expected to manifest likewise in the  $p_T$  reach of the nuclear modification factors. The raw  $p_T$  distributions measured after the event and track selection are affected by several detector effects which must be corrected for. The corrections are implemented using the information of MC simulations provided by the ALICE collaboration. In some cases, imperfections of these simulations must be corrected with data-driven approaches.

The  $p_{\rm T}$  distributions are normalized by the number of inelastic events  $N_{\rm INEL}$ . Due to the existence of a trigger  $e_{\rm Trig}$  and a vertex reconstruction  $e_{\rm Vz}$  efficiency, the reconstructed number of events  $N_{\rm ev}^{\rm rec}$  represents only a fraction of  $N_{\rm INEL}$ . To correct  $N_{\rm ev}^{\rm rec}$ ,  $e_{\rm Trig}$  and  $e_{\rm Vz}$  must be determined. Note that these efficiencies have been observed to be unity in Pb-Pb collisions. The correction is thus implemented only in pp collisions.

Because of the trigger and vertex efficiency, a correction for the tracks from the corresponding missing events is needed. This signal loss is calculated using MC simulations.

The overall efficiency, which results from the tracking efficiency and the geometrical acceptance, is determined using the information provided by the MC simulations. It has the largest effect among all corrections on the  $p_{\rm T}$  distributions. Since the overall efficiency is particle dependent, the data-driven approach develop in [Huh17] is used to correct for the underestimation of strange particles present in MC simulations. The correction is implemented by reweighting the overall efficiency with the relative abundance of each particle type. The reweighting factors are taken from the cited work.

Furthermore, the  $p_{\rm T}$  distributions are corrected for the contamination by secondary particles, which is estimated by MC simulations. The underestimation of strange particles, which also affects the contamination, is redressed by scaling the contamination obtained from pure MC with  $p_{\rm T}$ -dependent factors extracted from the parametrization of DCA<sub>xy</sub> distributions from data using MC templates. Moreover, the measured  $p_{\rm T}$  distributions are smeared due to the effect of the  $p_{\rm T}$  resolution. The smearing is more pronounced in the high  $p_{\rm T}$  region of the  $p_{\rm T}$  spectra. In the framework of a toy MC simulation, the required  $p_{\rm t}$ -dependent correction factors are calculated by means of the ratio of the true  $p_{\rm T}$  distributions, obtained from the previous ALICE measurements of  $R_{\rm AA}$ , to  $p_{\rm T}$  distributions smeared due to the  $p_{\rm T}$  resolution.

In this thesis, the systematic evaluation of uncertainties focuses on the assumptions made for the track selection criteria. Additional sources of systematic uncertainties are also reported, but they have not been evaluated in this work since further studies are required.

After the implementation of the mentioned corrections, the fully corrected  $p_T$  spectra of primary charged particles are calculated for pp collisions and for the studied Pb-Pb centrality classes. The results in pp collisions are expressed in form of a differential cross section, while the ones in Pb-Pb are given as invariant yields. The  $p_T$  spectra present a steeply falling shape at high  $p_T$ . In Pb-Pb collisions, a strong centrality dependence is observed. The obtained results show a good agreement with the previous ALICE measurement, reported in [AAA<sup>+</sup>18], within the systematic uncertainties. In pp collisions, an improvement in terms of  $p_T$  reach as well as granularity is accomplished at high  $p_T$  due to the increased statistics in the used data sets.

To conclude, the nuclear modification factors are calculated for nine centrality classes in Pb-Pb collisions. These are in good agreement with the previous ALICE measurement, within the systematic uncertainties. As expected, a suppression of the charged-particle production is observed, specially towards central collisions. The increased statistics in pp collisions allow for an enlarged  $p_{\rm T}$  reach and higher granularity in the high  $p_{\rm T}$  region in the nuclear modification factors. This fact enables a better distinction between theoretical models.

# Appendices

## A Kinematic variables

In experimental high-energy physics, the Cartesian coordinates, in which z represents the beam axis, are substituted by spherical coordinates to describe the momentum. It follows  $\vec{p} = (|p|, \theta, \phi)$ , where  $\theta$  is the emission angle of the particle production relative to the beam axis and  $\phi$  the azimuthal angle. In this context, it is preferred to use relativistic variables which describe conveniently processes that undergo Lorentz transformations. For instance, the pseudorapidity  $\eta$  is used as spatial coordinate to characterize the angle  $\theta$  as follows [Bü18]:

$$\eta = -\ln\left(\tan\frac{\theta}{2}\right) \tag{A.1}$$

Due to conservation laws, the momenta measured transverse to the beam axis must originate after the particle collisions. Therefore, it is considered advantageous to use as coordinate the transversal momentum  $p_T$  of the produced particle defined as [Bü18]:

$$p_{\rm T} = |p| \cdot \sin \theta \tag{A.2}$$

The transversal momentum is invariant under Lorentz transformation. As a result, the momentum is defined with  $\vec{p} = (p_T, \eta, \phi)$ .

## **Bibliography**

- [AAA<sup>+</sup>10] J. Alme, Y. Andres, H. Appelshäuser, S. Bablok, N. Bialas, R. Bolgen, U. Bonnes, R. Bramm, P. Braun-Munzinger, R. Campagnolo, P. Christiansen, A. Dobrin, C. Engster, D. Fehlker, Y. Foka, U. Frankenfeld, J.J. Gaardhøje, C. Garabatos, P. Glässel, and et al. The alice tpc, a large 3-dimensional tracking device with fast readout for ultra-high multiplicity events. *Nuclear Instruments and Methods in Physics Research Section A: Accelerators, Spectrometers, Detectors and Associated Equipment*, 622(1):316–367, 2010.
- [AAA<sup>+</sup>13] B. Abelev, J. Adam, D. Adamová, A. M. Adare, M. M. Aggarwal, G. Aglieri Rinella, M. Agnello, A. G. Agocs, A. Agostinelli, Z. Ahammed, and et al. *Centrality determination of Pb-Pb collisions atsNN*=2.76TeV with ALICE. Physical Review C, 88(4), Oct 2013.
- [AAA+18] S. Acharya, F. T.-. Acosta, D. Adamová, J. Adolfsson, M. M. Aggarwal, G. Aglieri Rinella, M. Agnello, N. Agrawal, Z. Ahammed, and et al. *Transverse momentum spectra and nuclear modification factors of charged particles in pp, p-Pb and Pb-Pb collisions at the LHC. Journal of High Energy Physics*, 2018(11), Nov 2018.
- [AAAR<sup>+</sup>17] D. Adamová, M. M. Aggarwal, G. Aglieri Rinella, M. Agnello, N. Agrawal, Z. Ahammed, S. Ahmad, S. U. Ahn, S. Aiola, and et al. *Production of*  $\sigma(1385)^{\pm}$  *and*  $\xi(1530)^{0}$  *in pPb collisions at*  $\sqrt{s_{\rm NN}}=5.02$  tev. *The European Physical Journal C*, 77(6), Jun 2017.
- [Agg21] Madan M. Aggarwal. *Elliptic Flow in Relativistic Heavy-Ion Collisions*. Springer Singapore, 2021.
- [ALI18a] ALICE 2017 luminosity determination for pp collisions at  $\sqrt{s} = 5$  TeV. Nov 2018.
- [ALI18b] *Centrality determination in heavy ion collisions.* Aug 2018.

- [BEK<sup>+</sup>17] Evan Bianchi, Jacob Elledge, Amit Kumar, Abhijit Majumder, Guang-You Qin, and Chun Shen. The x and  $q^2$  dependence of  $\hat{q}$ , quasi-particles and the JET puzzle, 2017.
- [Bjo82] J. D. Bjorken. Energy Loss of Energetic Partons in Quark Gluon Plasma: Possible Extinction of High p(t) Jets in Hadron Hadron Collisions. 8 1982.
- [BMW06] P. Braun-Munzinger and J. Wambach. Extreme Materie, Bei welchen Bedingung enentsteht in stark wechselwirkender Materie ein Quark-Gluon-Plasma? Physik Journal, 2006.
- [BV09] Amos Breskin and Rüdiger Voss. *The CERN Large Hadron Collider:* Accelerator and Experiments. CERN, Geneva, 2009.
- [Bü18] H. Büsching. Skript zur Vorlesung Kern- und Teilchenphysik 4b. University of Frankfurt, 2018.
- [CEK<sup>+</sup>16] Yang-Ting Chien, Alexander Emerman, Zhong-Bo Kang, Grigory Ovanesyan, and Ivan Vitev. Jet quenching from qcd evolution. *Phys. Rev. D*, 93:074030, Apr 2016.
- [CERa] CERN. CERN complex. https://commons.wikimedia.org/wiki/File:LHC.svg (accessed in Juli 2021).
- [CERb] CERN. CERN's accelerator complex. https://home.cern/science/accelerators/accelerator-complex (accessed in Juli 2021).
- [CERc] CERN. The Large Hadron Collider . https://home.cern/science/accelerators/large-hadron-collider (accessed in Juni 2021).
- [CERd] CERN. The Standard Model. https://home.cern/science/physics/standard-model (accessed in March 2021).
- [CERe] ROOT CERN. TFractionFitter Class Reference. https://root.cern.ch/doc/v606/classTFractionFitter.html (accessed in August 2020).
- [Che10] M. N. Chernodub. Background magnetic field stabilizes qcd string against breaking, 2010.
- [CJJ<sup>+</sup>74] A. Chodos, R. L. Jaffe, K. Johnson, C. B. Thorn, and V. F. Weisskopf. *New extended model of hadrons. Phys. Rev. D*, 9:3471–3495, Jun 1974.

- [col14] ALICE colaboration. *Performance of the ALICE experiment at the CERN LHC. International Journal of Modern Physics A*, 29(24):1430044, Sep 2014.
- [Col17] ALICE Collaboration. *The ALICE definition of primary particles*. Jun 2017. http://cds.cern.ch/record/2270008 (accessed in July 2021).
- [DBZ16] Magdalena Djordjevic, Bojana Blagojevic, and Lidija Zivkovic. *Mass tomography at different momentum ranges in quark-gluon plasma*. *Phys. Rev. C*, 94:044908, Oct 2016.
- [GEA] *Geant4—a simulation toolkit*, journal = Nuclear Instruments and Methods in Physics Research Section A: Accelerators, Spectrometers, Detectors and Associated Equipment, volume = 506, number = 3, pages = 250-303, year = 2003, issn = 0168-9002, doi = https://doi.org/10.1016/S0168-9002(03)01368-8, url = https://www.sciencedirect.com/science/article/pii/S0168900203013688, author = S. Agostinelli and J. Allison and K. Amako and J. Apostolakis and H. Araujo and P. Arce and M. Asai and et al.,.
- [GEL13] FRANÇOIS GELIS. Color glass condensate and glasma. International Journal of Modern Physics A, 28(01):1330001, Jan 2013.
- [Groa] Data Preparation Group. ALICE data flow. https://indico.cern.ch/event/666222/contributions/2768780/attachments/1551303/2437229/DPG\_AnalysisTutorial\_20171102.pdf (accessed in August 2021).
- [Grob] Data Preparation Group. Event normalization. https://twiki.cern.ch/twiki/bin/viewauth/ALICE/Eventnormalization (accessed in Mai 2021).
- [Gro18] Julius Gronefeld. Transverse Momentum Distributions and Nuclear Modification Factors in Heavy-Ion Collisions with ALICE at theLarge Hadron Collider. PhD thesis, Technische Universitaet Darmstadt, 2018.
- [Huh17] Patrick Huhn. Datenbasierte Effizienzkorrektur zum Nachweis geladener Teilchen im ALICE Experiment. Master's theis, University of Frankfurt, 2017.

- [Kni14] Michael Linus Knichel. *Transverse momentum distributions of primary charged particles in pp, p–Pband Pb–Pb collisions measuredwith ALICE at the LHC*. PhD thesis, Technische Universitaet Darmstadt, 2014.
- [LKd18] Constantin Loizides, Jason Kamin, and David d'Enterria. *Improved Monte Carlo Glauber predictions at present and future nuclear colliders. Phys. Rev. C*, 97:054910, May 2018.
- [Mai15] Antonin Maire. *Phase diagram of QCD matter : Quark-Gluon Plasma*. General Photo, Jun 2015.
- [Man09] Robert Mann. *An Introduction to Particle Physics and the Standard Model*. Taylor and Francis Group, 2009.
- [MRSS07] Michael L. Miller, Klaus Reygers, Stephen J. Sanders, and Peter Steinberg. Glauber Modeling in High-Energy Nuclear Collisions. Annual Review of Nuclear and Particle Science, 57(1):205–243, 2007.
- [Nag13] Yorikiyo Nagashima. *An Introduction to Particle Physics and the Standard Model*. John Wiley and Sons, Incorporated, 2013.
- [PL18] Edgar Perez Lezama. *Transverse momentum spectra and cross sections of charged particles in pp collisions measured with ALICE*. PhD thesis, University of Frankfurt, 2018.
- [Por19] Gabriel Porebski. Einfluss der Zentralitätsbestimmung auf die trasnversalimpulsspektren geladenerTeilchen in ALICE. Bachhelor's theis, University of Frankfurt, 2019.
- [SMS08] Torbjörn Sjöstrand, Stephen Mrenna, and Peter Skands. *A brief introduction to PYTHIA 8.1. Computer Physics Communications*, 178(11):852–867, Jun 2008.
- [Sop97] Davison E. Soper. *Parton distribution functions*. *Nuclear Physics B Proceedings Supplements*, 53(1-3):69–80, Feb 1997.
- [SSS09] Sourav Sarkar, Helmut Satz, and Bikash Sinha. *The physics of the quark-gluon plasma: introductory lectures*, volume 785. Springer, 2009.
- [T<sup>+</sup>18] M. Tanabashi et al. *Review of Particle Physics*. *Phys. Rev. D*, 98(3):030001, 2018.
- [Tau17] Arturo Tauro. *ALICE Schematics*. abrufbar auf: http://cds.cern.ch/record/2263642 (Februar 2019), May 2017.

- [vdM68] S van der Meer. Calibration of the effective beam height in the ISR. Technical report, CERN, Geneva, 1968.
- [Ven08] Raju Venugopalan. From glasma to quark–gluon plasma in heavy-ion collisions. Journal of Physics G: Nuclear and Particle Physics, 35(10):104003, Sep 2008.
- [Wel] Pipa Wells. Tracking at the LHC. https://indico.cern.ch/event/96989/contributions/2124495/attachments/1114189/1589705/WellsTracking.pdf (accessed in April 2021).
- [WG91] Xin-Nian Wang and Miklos Gyulassy. hijing: A Monte Carlo model for multiple jet production in pp, pA, and AA collisions. Phys. Rev. D, 44:3501–3516, Dec 1991.
- [Wie08] Jens Wiechula. *Commissioning and Calibration of the ALICE-TPC*. PhD thesis, University of Frankfurt, 2008.
- [Wik] Wikipedia. Sagitta (geometry). https://en.wikipedia.org/wiki/ Sagitta\_(geometry) (accessed in March 2021).
- [XLG15] Jiechen Xu, Jinfeng Liao, and Miklos Gyulassy. *Consistency of Perfect Fluidity and Jet Quenching in Semi-Quark-Gluon Monopole Plasmas. Chinese Physics Letters*, 32(9):092501, Aug 2015.

## Acknowledgments

First and foremost, I have to thank Prof. Dr. Henner Büsching for giving me the opportunity of writing my master's thesis under his supervision. In addition, I would like to thank him for his guidance, his kind counsel, and, specially, for his patience.

In addition, I would like to give thanks to Prof. Dr. Harald Appelshäuser, who accepted to be the second examiner of this work.

I would like to acknowledge my tutors, Patrick Huhn and Mario Krüger. Their wise advice and the daily discussions with them played a crucial role that helped me to complete successfully this thesis.

In addition, I would like to thank Prof. Dr. Anton Andronic and Dr. Kai Schweda for their willingness to help me whenever I had questions regarding the analysis.

Furthermore, many thanks to the entire High Energy Physics working group from Frankfurt for all the wonderful moments.

Finally, my special thanks go to my parents and my siblings for their moral support and encouragement throughout this time. None of this could have happened without their unconditional love.

## Eigenständigkeitserklärung

Hiermit erkläre ich, dass ich die Bachelorarbeit selbstständig und ohne Benutzung anderer als der angegebenen Quellen und Hilfsmittel verfasst habe. Alle Stellen der Arbeit, die wörtlich oder sinngemäß aus Veröffentlichungen oder aus anderen fremden Texten entnommen wurden, sind von mir als solche kenntlich gemacht worden. Ferner erkläre ich, dass die Arbeit nicht -auch nicht auszugsweise- für eine andere Prüfung verwendet wurde.

Frankfurt am Main, 13.09.2021

Youssef El Mard Bouziani